ADVANCED MATERIALS INTERFACES
www.advmatinterfaces.de

^{129}Xe NMR on Porous Materials: Basic Principles and Recent Applications

*Dorothea Wisser and Martin Hartmann**

A large number of functional and catalytic materials exhibit porosity, often on different length scales and with a hierarchical structure. The assessment of pore sizes, pore geometry, and pore interconnectivity is complex and usually not feasible by classical spectroscopic and diffraction techniques. One of the most powerful methods to probe these parameters is nuclear magnetic resonance (NMR) spectroscopy of xenon, which is introduced into the pore system. Adsorbed to the pore walls, it acts as probe nucleus. In this tutorial review, an introduction into the basic principles of ^{129}Xe NMR spectroscopy and the models developed to determine pore sizes in different materials are given. The possibilities and limitations of this method for obtaining insights into hierarchical structures of functional materials are highlighted and a review of recent works is presented.

1. Introduction

Similar to all noble gases, xenon (Greek: ξενοσ—foreign, strange) is a colorless, odorless, dense, unreactive gas. It is present only in trace amounts in the earth atmosphere. Among the seven stable isotopes, ^{129}Xe has a relatively high natural abundance of 26.4%. The nuclear spin of this isotope is 1/2, rendering it well suited for detection in nuclear magnetic resonance (NMR) spectroscopy. Also ^{131}Xe can be detected by NMR, but yields more complex spectra due to the quadrupolar nature of the nucleus with a spin 3/2.[1,2] The Larmor frequency of ^{129}Xe is ≈10% higher than that of ^{13}C, thus situated in the middle of the accessible range of nuclei. Its receptivity, taking into account the natural abundance, is around 32 times higher than the value for ^{13}C, making ^{129}Xe overall a convenient nucleus to study by NMR spectroscopy.[3]

With 54 electrons, xenon has the largest electron cloud among the noble gases, except radon, which is however subject to radioactive decay. The large electron cloud makes xenon strongly polarizable in magnetic fields, leading to large chemical shifts of up to 7000 ppm. The sensitive dependence of the chemical shift on the chemical environment combined with its inertness render ^{129}Xe an ideal NMR probe nucleus.

The use of xenon as probe molecule for the NMR investigation of porous materials was first demonstrated in the 1980s by Ito and Fraissard on zeolites,[4] showing that the chemical shift of xenon was influenced by the pore size and the presence of cations. In 1981, Ripmeester and Davidson investigated the chemical shift of xenon clathrate hydrate (caged xenon in solid water).[5] Since, ^{129}Xe NMR has become an important tool to study the pore systems of numerous materials including zeolites, mesoporous silicas, aluminas, polymers, porous organic molecules, and metal–organic frameworks (MOFs). ^{129}Xe NMR allows to probe pore sizes, but also pore connectivity or pore blocking. These parameters make the technique particularly interesting for the investigation of hierarchical functional materials, namely materials with interconnected pores on different length scales. Catalysts such as zeolites with a hierarchical overall pore structure are increasingly prepared in order to optimize mass transport throughout the particles and thus improve the performance of the catalyst.[6]

In the first part of this tutorial review, we describe the fundamentals of ^{129}Xe NMR for the investigation of porous materials, the existing models for different material classes, and its applications to the study of hierarchical materials, emphasizing the information that can be obtained from the spectra. In the second part, we review the most recent developments and applications in the field in order to exemplify the benefits and challenges of this technique.

2. Theory and Basic Principles of ^{129}Xe NMR

2.1. The NMR Experiment

Solid-state NMR spectroscopy has proven to be an indispensable tool for the analysis of the structure and dynamics of solid materials.[7] It is often used in parallel with other techniques such as X-ray crystallography, powder X-ray diffraction and ab initio calculations which link NMR parameters with structure. Solid-state NMR techniques are sensitive to the local environment of nuclei and capable of detecting changes in bond angles, bond lengths, and molecular dynamics.[8] The basics of NMR is the behavior of the magnetic moments of certain atomic nuclei influenced by an external magnetic field and local fields, created by surrounding nuclei and the electric charge distribution around the nuclei. The basis for a deeper understanding and interpretation of NMR spectra of solid powder samples

Dr. D. Wisser, Prof. M. Hartmann
Erlangen Center for Interface Research and Catalysis (ECRC)
Friedrich-Alexander-Universität Erlangen-Nürnberg
Egerlandstrasse 3, 91058 Erlangen, Germany
E-mail: martin.hartmann@fau.de

The ORCID identification number(s) for the author(s) of this article can be found under https://doi.org/10.1002/admi.202001266.

DOI: 10.1002/admi.202001266

is the examination of the various magnetic interactions in an ensemble of nuclear magnetic moments.[9] Typically, four types of spin interactions have to be considered in order to explain the NMR spectra of a diamagnetic solid sample.

1) The chemical shift, which is a consequence of the shielding of the applied external magnetic field by the electrons surrounding the nucleus. The electron movement creates a weak additional internal magnetic field, typically opposing the external magnetic field. The nucleus thus experiences a modulated (typically reduced) overall magnetic field.
2) The magnetic dipole–dipole interactions between nuclear magnetic moments, which are a function of the distance of the two nuclei.
3) The indirect nuclear spin–spin coupling, often called J-coupling, which is mediated by the electron clouds surrounding the two nuclei.
4) The nuclear electric quadrupolar interaction for nuclei with spin I > ½, which is due to the electrical interaction between the nuclear quadrupole moment of a nucleus possessing non-spherical electrical charge distribution and the electric field gradient at the site of the nucleus.

2.2. The ^{129}Xe Chemical Shift

The chemical shift of xenon confined in a porous material is a function of pressure and temperature. It is expressed as the sum of several terms:

$$\delta = \delta_0 + \Delta_{Xe-Xe} \cdot \rho_{Xe} + \delta_S + \delta_{SAS} + \delta_E + \delta_M \quad (1)$$

δ_0 being the chemical shift of gaseous xenon at zero pressure, which is set to 0 by convention and used as reference. As a signal at zero xenon pressure can obviously not be measured directly, it is obtained in practice by recording the chemical shifts of the gas phase at different pressures and extrapolation to 0. δ_0 is weakly temperature dependent in the typical experimental range of 250–400 K.[10] The second term describes the contribution of xenon–xenon interactions in the gas phase, which increase with the xenon density ρ_{Xe}.[11,12] Both terms are a function of temperature.[13] δ_S contributes the xenon–surface interactions, which are central for the investigation of porous materials, and will be described in detail in Section 2.3. δ_S usually decreases with increasing temperature, as with increasing thermal energy, the residence time of xenon atoms adsorbed on the pore wall will be reduced. (Only in the particular case of xenon confined in pores that are about the size of the xenon atom, xenon will be held in the center of this pore by rapidly growing repulsive forces at very close distances to the pore walls. Here, thermal movement will bring xenon inevitably closer to the pore walls, its chemical shift thus increases with increasing temperature.[14]

δ_{SAS} describes the influence of strong adsorption sites (SAS). Xenon will spend a lot of time adsorbed on those sites, leading to very large chemical shift contributions. SAS can be recognized by an increase of δ at very low xenon pressure, as most xenon is then adsorbed on these sites. In contrast, in the case of weak adsorption δ will approach 0 at low xenon pressure. SAS are often charged sites or paramagnetic cations, for example, Pt nanoparticles confined in a NaY zeolite, Mg^{2+}, Sr^{2+}, or $Cu^{+/2+}$ ions exchanged into a zeolite or isolated vanadyl sites on a TiO_2 catalyst.[15–18] Additionally, electric fields induced, for example, by ions in the structure add a contribution δ_E to the chemical shift.[13] Likewise, paramagnetic components induce an additional shift δ_M. Both effects can be active even if xenon is not directly adsorbed on such a site. In the literature, equations similar to (1) may be found in which some of the terms are grouped or omitted. The behavior of these last parameters with temperature has been studied in less detail. Not specifically included in Equation (1), but possibly relevant are interactions of xenon with π orbitals of aromatic molecules, as shown by density functional theory calculations and infrared spectroscopy.[19]

All chemical shifts are considered to be averaged to their isotropic value. This is the case if xenon atoms can move freely inside a pore. In very confined surrounding such as organic cages or narrow channels[20,21] of a size close to the diameter of the xenon atom, anisotropic signal shapes are observed.[13] In that case, simulations using molecular models will be extremely useful to draw a picture of the geometry of the environment. A recent example of models for xenon in confinement, allowing for the prediction of chemical shifts, can be found in Section 4.4.

2.3. Models for Pore size Determination Using ^{129}Xe NMR

Although the description of the chemical shift has previously been introduced as a sum of several contributions, the observed chemical shift in a real system is the weighted average of all contributions the ^{129}Xe nucleus experiences on the time scale of an NMR experiment (on the order of milliseconds). Therefore, for practical applications, Equation (1) needs to be simplified by assuming the absence of SAS, electronic or paramagnetic effects. Furthermore, at sufficiently low pressure, gas phase xenon–xenon interactions can be neglected. Importantly, at room temperature, xenon atoms exchange quickly between different adsorption sites and the gas phase, implying that during the NMR experiment, they are able to move from the gas phase to an adsorption site or vice versa. This phenomenon is called chemical exchange (in contrast to nuclear spin exchange). The observed chemical shift is therefore averaged between the gas phase signal and the chemical shift of xenon adsorbed on a specific site, both multiplied by the respective molar fractions. For the case of a single adsorption site, this yields:

$$\delta = \delta_S = X_a\ \delta_a + X_g \delta_g \quad (2)$$

$$X_a = \frac{n_a}{n_a + n_g} \quad (3)$$

X_a and X_g being the populations of the adsorbed and the gas state, and δ_a the chemical shift of adsorbed xenon, which cannot directly be measured. (In some works, δ_a is labeled as δ_S,[22,23] here the nomenclature δ_a is used). At low xenon pressures, δ_g is 0. In most spectra, a signal of gaseous xenon in the excess gas phase between the particles is therefore visible at 0 ppm. The free gas is not or only slowly exchanging with adsorbed xenon.

2.3.1. Zeolites

In 1987, Demarquay and Fraissard introduced the first model for the dependence of the ^{129}Xe shift on the pore size.[24] This model was empirically established on a series of dealuminated zeolites or zeolites containing only sodium cations as counter ion with different pore sizes. It is, thus, only strictly valid for this class of materials possessing micropores or small mesopores (pore diameters ranging from 1 to 4 nm). They determined the mean free path $\overline{l}$ of xenon within the pores to

$$\delta_S = \delta_a \cdot \frac{a}{a+\overline{l}} \tag{4}$$

with a being a material-dependent coefficient. Plotting $1/\delta_S$ as a function of $\overline{l}$, a linear correlation was obtained

$$\frac{1}{\delta_S} = \frac{1}{\delta_a} + \frac{\overline{l}}{a \cdot \delta_a} \tag{5}$$

From fitting the experimental data with this correlation, δ_a = 243 ppm and a = 2.054 Å were extracted to establish the equation

$$\delta_S = 243\,\text{ppm} \cdot \frac{2.054\,\text{Å}}{2.054\,\text{Å} + \overline{l}} \tag{6}$$

In order to determine the pore diameter from the mean free path, the pore geometry needs to be known, which can be established by following the pressure dependence of the chemical shift. For spherical pores in the absence of SAS, a linear correlation exists between chemical shift and the xenon concentration, while for anisotropic cylindrical pores the correlation is curved. The pore diameter can thus be extracted from the chemical shift at zero xenon pressure.

$D_c = \overline{l} + 4.4$ Å for cylindrical pores, and
$D_s = 2 \cdot \overline{l} + 4.4$ Å for spherical pores.[24]

2.3.2. Mesoporous Silica

The group of Mastikhin developed an analogous model for mesoporous silica materials, which again do not contain paramagnetic sites or SAS.[22,23] They started by determining the number of adsorbed atoms n_a from Henry's law:

$$n_a = KpS \tag{7}$$

where S is the specific surface area of the pore, p the pressure, and K the Henry constant. Assuming ideal gas behavior, Equation (7) allows to calculate the number of atoms in the pore gas phase as

$$n_g RT = pV \tag{8}$$

V being the pore volume, R the gas constant, and T the temperature. Combining (2), (3), (7), and (8), assuming that at low xenon pressures δ_g is 0, one can simplify

$$\delta = \frac{\delta_a}{1 + \frac{V}{SKRT}} \tag{9}$$

Note that here, δ is equivalent to δ_S as in Equation (2). In (9), the observed chemical shift does not depend upon the equilibrium pressure.[22] If δ_a is known for the specific material, it is possible to obtain the volume-to-surface ratio, V/S. The relation between the pore diameter D and the local volume-to-surface ratio can also be written as a function of pore geometry

$$\frac{V}{S} = \frac{D}{\eta} \tag{10}$$

with η = 4 in a cylindrical pore model, η = 2.8 for randomly packed spheres of equal size and η = 2 for a slit-like pore model. Thus Equation (9) can be written as

$$\delta = \frac{\delta_a}{1 + \frac{D}{\eta KRT}} = \frac{\delta_a}{1 + \frac{D}{b}} \tag{11}$$

The authors investigated a series of silica gels, porous silica glasses, and periodic mesoporous organosilicas (PMO) with known pore diameters between 0.5 and 40 nm, but with differing pore topologies and surface chemistries. They were able to generalize Equation (11) by fitting the experimental data with nonlinear least-squares fits. The experimental data of all four material classes mentioned above could be described with a single fit using δ_a = 116 ± 3 ppm and b = 117 ± 8 Å. However, the experimental data of the single material classes were also fitted separately (**Table 1**). It should be noted that the form factor η only has a small effect on the results. For sol–gel and colloidal silica, the group of Malier found significantly different fit parameters (Table 1, line 5).[25] Note that in practice, the applicability of this model will be limited if the material

Table 1. Overview of experimentally determined values for δ_s and b for different materials.

Entry	Material	δ_a [ppm]	b [Å]	D [Å]	Pore network	Ref.
1	Silica gel	118 ± 5	122 ± 12	21–396[c]	Interparticular voids	[23]
2	Porous glass	97 ± 6	130 ± 18	44–387	3D pore network	[23]
3	PMO[a]	112 ± 2	115 ± 16	6–32[c]	Hexagonal arrangement of cylindrical pores[26]	[23]
4	PMO[b]	118 ± 2	143 ± 17	6–44[c]	Hexagonal arrangement of cylindrical pores or cubic 3D pore network[26]	[23]
5	Sol–gel and colloidal silica	85 ± 3	117 ± 13	20–250[c]	Cylindrical pores	[25]

[a]Synthesized at room temperature; [b]Synthesized under solvothermal conditions, thus containing fewer unreacted silanol groups; [c]Determined from N_2 physisorption at 78 K.

exhibits a broad particle sizes distribution and, thus, a distribution of inter-particular mesopores with different size, which will result in a broadened xenon signal.[23]

2.3.3. AlPOs

Single-file diffusion of xenon atoms in narrow pores, with diameters just above the atom diameter, were initially studied by Meersmann et al., including the interpretation of xenon signal line shapes as function of the channel size.[27] Deng and co-workers further developed this model for the extraction of the pore size.[28] They validated the model for a range of different materials possessing 1D channels with a diameter less than twice the molecular size of a xenon atom, including AlPOs, SAPOs, aluminum-containing zeolites as well as aluminum-free silicalite. The model contains the evaluation of Xe–Xe interactions and thus δ_{Xe-Xe}, as initially proposed by Guizard and co-workers.[29] It is valid in the linear region of the pressure dependence, assuming that only collisions between two xenon atoms occur. For gaseous xenon, the chemical shift is defined as

$$\delta = \delta_0 + \delta_1 \cdot \rho_{Xe} \tag{12}$$

ρ_{Xe} describes the xenon density in amagat, the density unit of a perfect gas at standard conditions, 1 amagat = 0.044615 mmol cm^{-3}. δ_1 is defined here as a pressure-dependent chemical shift, δ_1 = 0.548 ppm per amagat. For Xe adsorbed in microporous materials, δ_{Xe-Xe} can be obtained from the density dependence of Equation (1). The ratio of collision frequency for xenon in the gas phase and in a 1D channel is further defined as

$$\frac{\overline{z}_{pore}}{\overline{z}_{gas}} = \frac{\delta_{Xe-Xe}}{\delta_1} = \frac{1}{2}\left(\frac{r}{d_{Xe}}\right)^2 \tag{13}$$

assuming similar xenon densities in the gas and inside the 1D channel. $\overline{z}$ is the collision frequency in the pore and in the free gas, r the channel radius, and d_{Xe} the xenon atomic diameter. Thus, the radius of the channel can be calculated using

$$r = \sqrt{\frac{2 \cdot \delta_{Xe-Xe}}{\delta_1}} \cdot d_{Xe} \tag{14}$$

The only restriction being that $\delta_{Xe-Xe} < \frac{0.274 \text{ ppm}}{\text{amagat}}$, again defined as a pressure-dependent term. The equation is thus only applicable for pores with a diameter of less than 0.88 nm. This model can also be applied to spherical pores, still providing reasonable pore size values.

2.3.4. Porous Carbons

Extraction of a precise pore diameter from carbon materials is more difficult than for well-defined crystalline substances, due to the heterogeneity of the materials and possible paramagnetic impurities. Fraissard and co-workers developed an empiric formula for a set of activated carbons based on their previous model on zeolites.[30–32] A linear correlation between δ_{Xe-Xe} and the mean pore diameter D was observed

$$D = \frac{\delta_{Xe-Xe} - 5.1 \text{ ppm} \cdot \text{mmol}^{-1}}{7 \text{ ppm cm}^3 \text{ mmol}^{-1} \text{ nm}^{-1}} \tag{15}$$

δ_{Xe-Xe} is expressed here in ppm cm^3 mmol^{-1}. Note that from this general expression, no information about the pore shape can be obtained. The authors stress, however, that δ_{Xe-Xe} is a better descriptor for the pore size in the micropore region for both siliceous and carbon materials than the chemical shift extrapolated to zero xenon pressure δ_S.

It is important to emphasize that all models discussed above are strictly only valid for a given class of materials. Moreover, a proper correlation between δ_{Xe-Xe} or δ_S and the pore diameter has to be established for each class. The models should only be extrapolated to closely related materials and conclusions should be drawn with care.

2.4. Hyperpolarization Methods

Measuring ^{129}Xe NMR spectra at very low gas pressures allows to obtain the chemical shift of the gas phase, which can be set to 0 in good approximation, and is used as reference. δ_S without the influence of xenon–xenon interactions can also be obtained. This approach however results in very long measurement times due to the inherently low sensitivity of the method, in particular in materials with low surface area. Additionally, at low xenon pressure the relaxation times T_1 can become very long. To overcome this limitation, hyperpolarization methods have been introduced, which drive the xenon polarization away from the Boltzmann equilibrium distribution

$$\frac{N_+}{N_-} = e^{-\frac{\gamma h B_0}{2\pi k_B T}} \tag{16}$$

N_+ and N_- being the number of spins parallel or antiparallel to the external magnetic field with a magnetic flux density B_0, γ the gyromagnetic ratio of the nucleus under study, h the Planck constant, k_B the Boltzmann constant, and T the temperature. This results in a significant increase of the net nuclear polarization and the signal intensity. The predominant approach for the hyperpolarization of xenon is the so-called Spin Exchange Optical Pumping (SEOP), in which xenon, often in a mixture containing nitrogen and a small amount of helium, is contacted with a rubidium gas.[33,34] In SEOP, Rb is vaporized at 100–150 °C and low pressure and placed in a magnetic field. It is irradiated by a circularly polarized light from laser diode arrays with a wavelength corresponding to the D_1 line of Rb. The spin angular momentum of the circularly polarized photons is transferred to valence electrons in vaporized Rb atoms, generating a polarized Rb spin population. This polarization is transferred to xenon upon collision of Rb atoms with xenon atoms by electron–nuclear hyperfine interactions, yielding a very high xenon polarization far from the Boltzmann equilibrium.[35–37]

Nitrogen is added to the gas mixture in order to quench photon emission from excited Rb atoms by transformation into

vibrational energy. A high laser power with a narrow linewidth is favorable for a high pumping rate. In batch production of HP xenon, very high polarizations can be achieved, leading to high experimental sensitivity, which allowed, for instance, for the detection of a sub-monolayer of xenon adsorbed on flat Ir single-crystal surface.[38] However, measurement times are limited by the relaxation of ^{129}Xe during T_1. Continuous flow set-ups were therefore implemented.[39] Continuous flow HP xenon production has also been coupled to MAS NMR.[40]

As an alternative to SEOP, hyperpolarization by cooling xenon gas to very low temperatures below 25 mK in the so-called brute force approach is possible.[41,42] Recently is has been shown that HP xenon can be produced in a dissolution dynamic nuclear polarization (d-DNP) polarizer. A frozen pellet of xenon dissolved in a glass-forming matrix containing a stable organic radical is prepared. Electron polarization of the unpaired electron is then generated by a high-power microwave and the electron polarization is transferred to xenon nuclear polarization. Xenon is then quickly heated to room temperature and is ready for injection into an in vivo scanner. The magnetization of xenon is comparable to that produced by SEOP.[43] However, the hyperpolarization decays with T_1 outside of the polarizer, as in SEOP batch approaches, thus limiting the measurement times.[43–45] For more aspects and details on the technical implementation of HP xenon NMR, we refer here to the excellent review by Gédéon and co-workers and the book chapter by the group of Sozzani.[36,46]

We also note here that in addition to applications in chemistry and material science, HP xenon is used as a probe nucleus in medical magnetic resonance imaging. Non-toxic and well tolerated, xenon introduced into the lungs will fill the lung voids and also dissolve in the tissue, giving distinct signals. The hyperpolarized state yields high signal intensity and thus high imaging contrast and serves as excellent probe of pulmonary structure and function, providing a non-invasive biomarker for a variety of respiratory diseases.[47,48]

2.5. 2D ^{129}Xe Exchange Spectroscopy

Xenon atoms in porous materials exchange between adsorption sites and the gas phase, either the free gas or gas in interparticle voids, or between different adsorption sites in pores of different size or surface chemistry. If the exchange rate between two states is faster than the NMR time scale, only a single resonance with weighted average shift will be detected (compare Equation (2)), a phenomenon named coalescence. Only if the exchange is slower than the NMR time scale, two signals will become visible. Reducing the temperature of an experiment decreases the exchange rates and may thus result in the resolution of different signals.

The chemical exchange between adsorbed xenon and the gas phase or between xenon in different pores can be visualized by the ^{129}Xe 2Dexchange spectroscopy experiment.[49,50] The straightforward pulse sequence (**Figure 1**a) results in a 2D spectrum exhibiting the peaks of xenon in the different pores along the diagonal. Off-diagonal cross peaks will appear if xenon exchanges between these pores during the exchange time τ (Figure 1b–d). The cross peak intensities are proportional to the number of xenon atoms exchanged. It is thus possible to record EXSY spectra with different mixing times and to determine the exchange rate by a first-order exponential fit of the signal intensity versus τ.[17,51] Sufficient spectral resolution of the individual cross peaks is however required.

3. Hierarchical Materials

Hierarchy in materials is defined with respect to their structure, by the combination of elements of different sizes with different properties or functions, with respect to transport of fluids or with respect to chemical (or biological) composition. In porous materials, a hierarchical pore system is beneficial with respect to transport of molecules. A hierarchical porous material contains interconnected pores of different sizes. A more strict sense of the term hierarchical requires smaller pores to branch off from larger pores (or vice versa), in order to ensure a splitting of the flow (or a recollection of the flow).[53]

Increasing efforts are made today to prepare microporous catalytic materials such as zeolites with an additional meso- or macropore structure in order to ensure short diffusion pathways and optimum mass transport. The accessibility of the active sites within a particle is thus improved, resulting in enhanced activity and/or reaction kinetics.[53] Hierarchical pore systems are introduced into these materials by several methods including hard and soft templating, co-templating, and etching yielding well-defined micropores and additional mesoporosity. The preparation pathways of such hierarchical all-zeolite materials mostly follow bottom-up approaches. In these approaches, the additional porosity is generated during a carefully designed and optimized crystallization procedure. In addition, some preparation routes follow top-down approaches, such as selective extraction of specific framework constituents from already synthesized microporous zeolites (e.g., via desilication). These approaches always include a post-synthetic step such as steaming, irradiation, leaching with either alkaline or acidic media or both.[53] This again facilitates mass transport toward more confined voids for separation or catalysis.[6] Furthermore, amorphous silica materials with ordered pore structures such as SBA-15 and PMO are excellent host materials for the functionalization with a variety of organic surface species and in some case may even be hierarchical with well-ordered mesoporosity and additional micro- or macroporosity.[54,55]

Pore connectivity cannot be probed by X-ray diffraction or spectroscopic techniques, including MAS NMR, while it is in principle possible by dedicated adsorption techniques such as *n*-nonane pre-adsorption or hysteresis scanning.[56,57] Also NMR diffusometry using pulse field gradients allows for the assessment of pore connectivity by introducing a liquid medium into the porous material. The group of Walsworth has extended this technique to ^{129}Xe gas diffusometry, allowing to probe gas diffusion coefficients and tortuosity on larger length scales > 50 μm.[58]

Related to NMR diffusometry is ^{129}Xe porometry introduced by Telkki et al.[59] Here, xenon is dissolved in a liquid, which is then imbibed by the material under study. Confined xenon within the liquid in pores of different sizes will give rise to different chemical shifts. When the sample is cooled and the

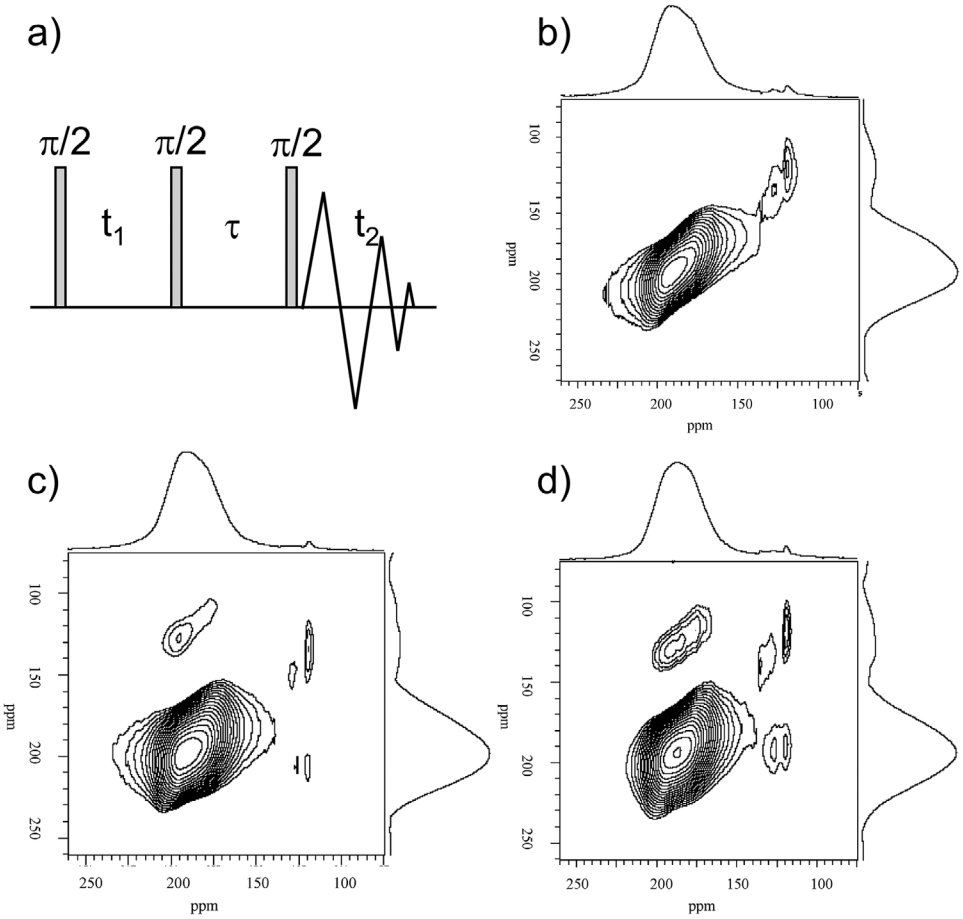

Figure 1. a) General EXSY pulse sequence. HP ^{129}Xe 2D-EXSY NMR spectra of mesoporous ZSM-5 at 143 K with different mixing times: b) 0.2 ms; c) 1 ms; d) 5 ms. Reproduced with permission.[52] Copyright 2008, American Chemical Society.

liquid starts to freeze, xenon is expelled from the freezing domains. As the melting point of a liquid depends on its confinement in a pore, the temperature at which a certain xenon signal disappears allows for conclusions about the pore size. In addition, pore size distributions are accessible by this method. Compared to ^{129}Xe in the gas phase, this technique, however, requires knowledge about the behavior of an additional liquid medium.

Possibly the best technique to probe pore connectivity is ^{129}Xe 2D EXSY. Exemplarily, the 2D EXSY HP ^{129}Xe spectra at 143 K with different exchange times of a ZSM-5 zeolite with a hierarchical pore structure is shown (Figure 1).[52] The zeolite was synthesized using tetrapropylammonium hydroxide and starch as co-templates, introducing mesopores into the structure. The diagonal peaks at 120 ppm in the 2D EXSY spectrum are attributed to xenon in the mesopores of the material, while the large peak around 190 ppm is ascribed to xenon in the micropores. The latter resonance is also observed for xenon in conventional, non-hierarchical ZSM-5. At an exchange time of 1 ms (Figure 1c), cross peaks appear, revealing chemical exchange between two pores with different sizes. For comparison, the authors prepared a physical mixture of conventional ZSM-5 and mesoporous silica material. In that material, cross peaks between micropores in the zeolite particles and mesopores in the silica particles only appeared after an exchange time of 5 ms (data not shown), indicating much slower inter-particle diffusion. In the spectrum of the hierarchical ZSM-5 recorded with 5 ms exchange time it is possible to discern two signals around 120 ppm, thus indicating two different kinds of mesopores. Whether they are interconnected remains unclear due to the low signal to noise ratio of the spectrum that may render cross peaks invisible. Obtaining sufficient signal intensity in a reasonable experimental time remains a limitation of the method.

Using ^{129}Xe EXSY, it is indeed also possible to confirm true hierarchy, that is, transport from the gas phase via larger pores into smaller ones. In the 2D EXSY HP ^{129}Xe spectra of CMK-3, a porous carbon material, three diagonal peaks are found for xenon in the gas phase, in mesopores and in micropores (**Figure 2**). Cross peaks were only observed between the gas phase and the mesopores (G;A) and between the meso- and micropores (A;B). This demonstrates gas transport from the larger into the smaller pores without significantly passing through the gas phase.[60] The effect of interconnected pores was also followed by loading CMK-3 with *n*-nonane. This caused the signal of xenon in micropores to disappear, and broadened the signal of the mesopores, which was interpreted as complete blocking of the micropores and partial narrowing of the mesopores with the adsorbate.[61]

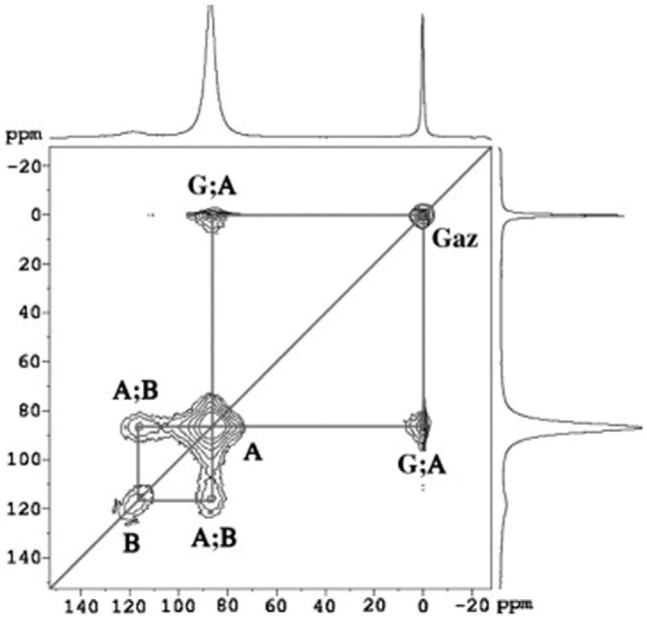

Figure 2. ^{129}Xe 2D-EXSYspectrum obtained on CMK-3 at 295 K (p = 53 kPa; mixing time = 50 ms). Reproduced with permission.[60] Copyright 2009, Elsevier.

Another prominent example for hierarchical materials is SBA-15, in which micropores branch off from the mesopores.[54,62,63] For this material, a single peak is observed as the xenon atoms are in fast exchange between the micro- and mesopores at room temperature.[64] This results in a peculiar behavior of the chemical shift which differs with the size of the micropores. Very short cylindrical micropores are prepared at high synthesis temperature (130 °C), and they accommodate only one or a few xenon atoms. In these pores, xenon is strongly adsorbed, which results in a nonlinear pressure dependence on the ^{129}Xe chemical shift. Larger micropores resulting from a low synthesis temperature (60 °C) induce a classical linear chemical shift behavior. In consequence, they do allow for xenon diffusion and are, thus, probably larger than twice the xenon atomic diameter (≈4 Å). In this way, information on the micropore size can be obtained in hierarchical systems even if the xenon signals from different pores are not resolved.

A number of hierarchical materials have been investigated in detail in the past years using ^{129}Xe NMR spectroscopy. Obviously ^{129}Xe 2D EXSY is a valuable tool to study the connectivity of different pores in MOFs, which are not hierarchical in the sense of a directed mass transport from larger to smaller pores.[65] Also the dynamic behavior of zeolitic imidazolium frameworks (ZIFs), a sub-class of MOFs, has been assessed.[66] Besides MOFs, amorphous porous organic polymers have gained great interest in recent years due to their thermal and chemical stability with tunable conductivity and chemical functionalities.[67,68] ^{129}Xe NMR was also used for the determination of porosity and connectivity in porous polymers.[69–72] EXSY spectra of porous polymers could be recorded in HP xenon continuous flow systems.[46,73] Further applications for the investigation of porous anode materials for Li ion batteries[74,75] and silica replicas of wood structures can be found.[76] Recently, it has been shown how the combination of the results of ^{129}Xe EXSY and PFG NMR diffusometry can yield information about porosity of materials over several length scales.[77]

4. Recent Applications

In addition to the more fundamental aspects discussed in the previous sections, selected examples from the most recent literature will be introduced here in order to exemplarily describe the benefits and challenges of ^{129}Xe for the characterization of porous materials and introduce novel developments in this area. For a thorough discussion of the literature prior to 2015, the reader is referred to excellent reviews and book chapters.[46,51,78–80]

4.1. Zeolites

The use of ^{129}Xe NMR for the investigation of porous solids began with studying the well-defined pore sizes of crystalline zeolites, and is still widely used today, as zeolites continue to be one of the most important classes of adsorbents and heterogeneous catalysts. Sensitive to specific adsorption sites and pore sizes, ^{129}Xe NMR in the past few years has served to elucidate the active sites available for catalysis in a zeolite, and helps to track and explain the catalytic activity, or poisoning of active sites and pore blocking. Novel zeolitic materials are designed with increasing complexity, by surface modification or by mixing two or more different types, in order to use the advantages of different zeolite types. Hierarchical structures are often introduced as they exhibit large meso- or macropores that facilitate diffusion and mass transport to the micropores for optimal use of the active sites.[53] Here again, ^{129}Xe has proven useful for studying the connectivity of the different pores and accessibility of the active sites.

A detailed mechanistic study of the behavior of adsorbed xenon gas in pristine SAPO-34 cubic crystallites was published by Liu and co-workers.[81] In this material with chabasite (CHA) topology, only one type of cages is present which are accessible through 8-membered ring windows. In a series of 1D ^{129}Xe NMR experiments on samples with different average Xe/cage loadings, the authors observed the evolution of strongly inhomogeneous signal shapes with increasing Xe loading (**Figure 3**). The signal shapes might indicate either the presence of Xe clusters with varying numbers of xenon atoms in the cages, or a chemical shift anisotropy of the adsorbed xenon. ^{129}Xe NMR spectra under MAS were carried out in order to average out anisotropic interactions. They revealed four resonances at a formal loading of one xenon atom per cage, each separated by about 4 ppm (Figure 3b). The chemical shift for xenon in SAPO materials has previously been calculated to 84 ppm for one xenon atom in the cage.[82,83] For zeolite NaA, the incremental increase in chemical shift had been found to be 20 ppm or more for each additional xenon atom in a cluster inside a cage.[84] The much smaller chemical shift separation observed here compared to zeolite NaA was explained by the authors by fast exchange between xenon atoms from clusters of different sizes, which is hindered in NaA by sodium cations partially blocking the pore entrances. The authors calculated that on average only

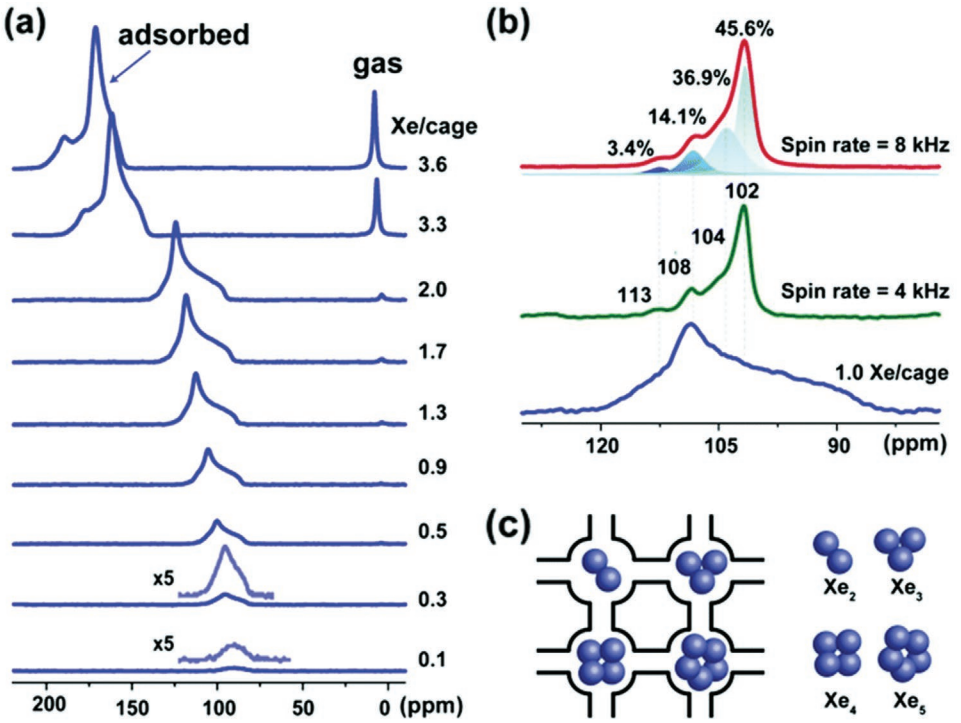

Figure 3. a) Loading-dependent ^{129}Xe NMR spectra of xenon adsorbed in the SAPO-34 molecular sieve at 298 K under static conditions. b) ^{129}Xe MAS NMR spectra at a spinning rate of 8 and 4 kHz and the corresponding static spectra of xenon adsorbed in SAPO-34 with an average loading of one atom per cage at 298 K. The fitting peaks are shown as color-filled from light to dark blue. c) Possible local structure of Xen clusters inside the CHA cages of SAPO-34. Reproduced with permission.[81] Copyright 2019, The Royal Society of Chemistry.

39% of the cages contain Xe and that the Xe clusters contain a maximum of five atoms, as determined from the cage size (Figure 3c). 2D EXSY spectra obtained from a higher loading (3.6 Xe atoms per cage on average) showed first cross peaks between Xe_5 clusters with the gas phase after an exchange time of 1 ms, cross peaks between the gas phase and smaller clusters after 2 ms, and finally exchange signals between smaller and larger clusters after 10 ms (**Figure 4**). From these data, the authors propose a model in which the crystallites are not homogeneously filled with xenon gas, and where at equilibrium, the number of xenon atoms per cage decreases from the outside to the inside of the particle (Figure 4d).

4.1.1. Studies on Active Sites in Zeolites and Catalytic Reactions

Bao and co-workers investigated the effect of pyridine adsorption in mordenite (MOR) upon the catalytic conversion of dimethyl ether to methyl acetate.[85] From ^{1}H MAS NMR spectra, the authors concluded that the smaller 8-membered ring pockets are not accessible, and pyridine adsorption takes place only in the larger 12-membered ring channels. An increasing pyridine content in these channels decreased the conversion rate of dimethyl ether, while the lifetime of the catalyst and the long-term selectivity of the reaction were increased. This was attributed to the higher selectivity for carbonylation of the Brønsted sites located in the smaller pockets compared to those in the channels. The 8-membered ring pockets remain free of pyridine and thus accessible for the substrate. ^{129}Xe NMR supported these findings: Xenon gas adsorbed in the channels and the pores showed distinct NMR resonances. Only the signal ascribed to xenon in the larger channels exhibited a dependence on the amount of pyridine adsorbed indicating that the mean free path of xenon is reduced by increased pyridine loading. Upon saturation of the zeolite with pyridine, the signals of ^{129}Xe in the pockets were not visible at room temperature indicating that the channels were completely blocked. Elevated temperatures (363 K) resulted in increased mobility of the guest molecules inside the zeolite and causing the signal of ^{129}Xe residing in the pockets to reappear.

^{129}Xe NMR spectra also suggested the existence of an adsorption site in MOR that may have been overlooked so far. Hou and co-workers studied the adsorption of HP ^{129}Xe on the zeolite mordenite at different temperatures.[86] Apart from the known ^{129}Xe resonances ascribed to xenon in 12-membered ring channels around 100 ppm and 8-membered ring pockets around 200 ppm, they also found a signal appearing only between 255 and 293 K with an intermediate chemical shift. 2D EXSY spectra were recorded with different mixing times, the cross peaks, indicative for exchange between the sites, deconvoluted and plotted as a function of mixing time. The exponential fit of these curves yields the characteristic exchange time of each cross peak. The chemical exchange rates for both the 12-membered ring channels with the newly found site and the 8-membered ring pockets with the new site were much faster than the exchange between channels and pockets. Therefore, the authors placed this new site at the intersection between channels and pockets.

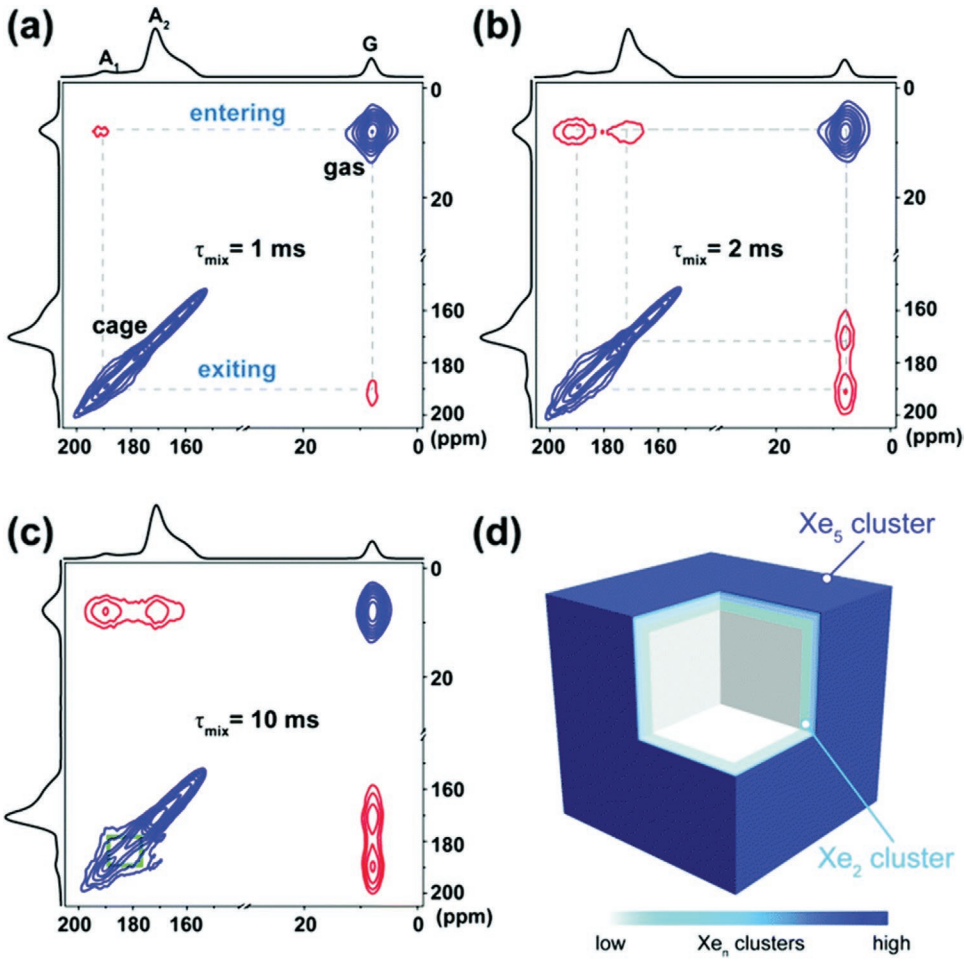

Figure 4. 2D EXSY NMR spectra of xenon adsorbed in the SAPO-34 molecular sieve with an average loading of 3.6 xenon atoms per cage at 298 K with mixing times of a) 1 ms, b) 2 ms, and c) 10 ms, respectively. The existence of cross peaks (red lines) indicates the xenon exchange between the gas phase and CHA cages of SAPO-34. The green dashed line represents the exchange between different adsorption sites in the micropores of SAPO-34. d) Possible spatial location of Xen clusters in a single SAPO-34 crystal. The colors from dark to light blue represent the decrease of the number of xenon per cage with the depth from the surface to interior. Reproduced with permission.[81] Copyright 2019, The Royal Society of Chemistry.

HP xenon gas was then introduced into the zeolite in an in situ set-up in a continuous flow together with methanol or water. The reduction of the ^{129}Xe NMR signal intensity confirmed that xenon was gradually replaced by methanol or water. For methanol, this replacement was faster for xenon gas adsorbed in the channels and at joint sites and slower for xenon in the pockets, an effect that the authors explain by a stronger affinity for methanol to the 12-membered ring channel sites (**Figure 5**a,c). For water on the other hand, the signal of xenon at the joint sites is replaced first (Figure 5b,d), indicating preferential affinity of water for these sites.

The group of Liu studied the coking mechanism and the localization of coke in a SAPO-34 catalyst during the methanol to olefin reaction.[87] Adsorbed xenon in the pores of the SAPO-34 material yielded a single signal, which decreased in intensity with increasing time on stream. This indicated that the coke formation is not uniform during the catalytic test and probably starts at the outside of the particles, thereby blocking the access of xenon gas to the pores. After 50 min, the remaining xenon signal was so weak that complete pore blocking was assumed. Other techniques such as nitrogen physisorption, electron microscopy, and infrared spectroscopy supported these findings.

A molybdenum-containing ZSM-5 zeolite modified with phosphate was studied by Bao and co-workers.[88] From solid-state NMR and XPS data, the formation of SAPO-like interfaces was suggested. ^{129}Xe NMR and nitrogen physisorption isotherms indicated a reduction of the pore size upon phosphate modification. The presence of phosphate increased the selectivity in methanol to olefin reaction and reduced byproduct formation, which the authors explained by a reduced density and strength of acid sites.

4.1.2. Studies on Mixed Phases and Hierarchical Zeolites

^{129}Xe NMR has been employed to probe the connectivity and accessibility of hierarchical structured zeolites. Valtchev and co-workers investigated the accessibility of sodalite cages in FAU zeolites after etching with NH_4F.[89] Those sodalite cages are not

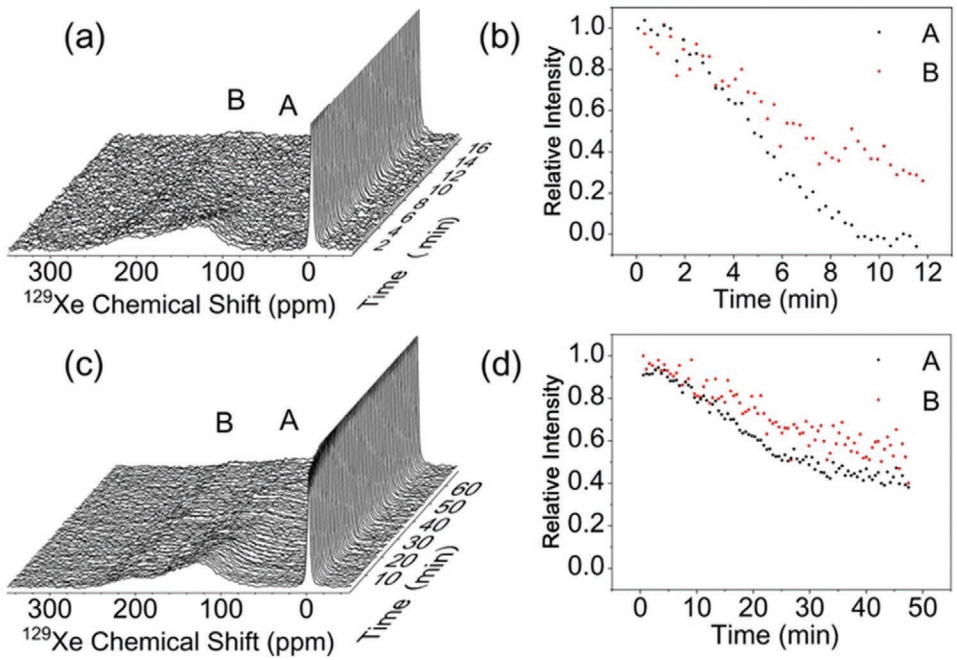

Figure 5. In situ ^{129}Xe NMR spectra recorded as a function of time during adsorption of a) methanol and c) water on H-MOR at 298 K; and time dependence of relative intensities of signal A (black) and signal B (red) for b) methanol and d) water adsorption process by deconvolution. Reproduced with permission.[86] Copyright 2019, American Chemical Society.

accessible in the pristine FAU, as the 6-membered ring windows connecting the small pores to the larger supercages are too small for xenon. The ^{129}Xe VT NMR spectra of the etched samples however showed a new, broad signal at low temperatures that was attributed to xenon adsorbed in the smaller sodalite cages. At room temperature, the presence of only one ^{129}Xe signal indicated fast exchange between the two sites.

Interlayer-expanded zeolites are hierarchical systems with improved accessibility to the zeolitic micropores. The group of Zhang studied such a material, obtained by introducing a silylation agent (dichlorodimethylsilane) as interlayer linker into a layered silicate, RUB-36, yielding a completely crystalline, layered porous material.[90] ^{29}Si CP NMR spectra showed the presence of Q^3 and Q^2 groups originating from the calcined silane linker. From cluster models, the authors calculated the chemical shift of xenon adsorbed at different sites in the interlayer-expanded zeolite, in particular in the 10-membered ring channels. They calculated large chemical shifts of 180 ppm for Xe adsorbed at SiOH groups at the interlayer linker in the channels, which is close to the measured chemical shifts of 205 ppm recorded at 173 K. Interlayer SiOH groups are thus probable sites for preferential Xe adsorption.

Another approach to increase the accessibility of active sites is to use amorphous zeolite seeds (3–4 nm in size) as so-called embryonic zeolites.[91] Embryonic ZSM-5 zeolites possess larger pore sizes than the corresponding crystalline zeolite as evidenced by a lower ^{129}Xe chemical shift. The xenon signal in the embryonic zeolites is narrower, pointing toward a more open structure and faster exchange. To take advantage of these properties, Valtchev and co-workers supported embryonic zeolites on a mesoporous silica-doped alumina matrix. The ^{129}Xe NMR spectrum of the composite showed a single resonance with a chemical shift in between the signal of pure ZSM-5 and the pristine matrix, highlighting the fast exchange between the embryonic zeolites and the matrix.

Upon partial dissolution of beta zeolite (BEA), a thin layer of silicalite-1 (MFI) recrystallizes on the surface of the BEA, leading to a hierarchical material.[92] The newly formed MFI layer is not observable in X-ray diffraction, but ^{129}Xe NMR allows for its detection. Besides the resonance at 100 ppm, characteristic for zeolite beta, a second small signal at around 135 ppm appears at temperatures below 270 K, corresponding to that of xenon adsorbed on silicalite-1.

The group of Xu introduced a series of composite zeolites by mixing seeds of ferrierite (FER) and MOR zeolites trying to combine favorable catalytic properties of both catalysts.[93] On the basis of ^{129}Xe NMR spectra, the authors claimed to obtain a better pore connectivity and higher adsorption capacity in the composite than in the case of a physical mixture of the two zeolites.

4.2. Mesoporous and Layered Silicas

Materials based on amorphous silica are ubiquitous in materials science and catalysis due to the versatile processability, thermal stability, and straightforward chemical modification of silica surfaces. Bao and co-workers compared the adsorption of water on zeolite ZSM-22 and on the mesoporous silica materials MCM-41 and SBA-15.[94] In an in situ NMR set-up, dry methane or methane gas saturated with water was flown through the samples while recording ^{1}H-NMR spectra online. In all materials, in the presence of water a reduced methane adsorption was detected. The crystalline zeolite ZSM-22, which

has the smallest pore size, showed the highest adsorption capacity for methane and the lowest for water. The time needed to reach water adsorption equilibrium was also the shortest for ZSM-22. The mesoporous silica SBA-15 behaved similarly to ZSM-22, whereas in MCM-41, the water content increased at a steady rate. In a second step, a HP Xe flow was introduced and ^{129}Xe NMR spectra were recorded alternating with ^{1}H NMR spectra. A competitive adsorption of water, slowly replacing adsorbed Xe was observed in all materials. Once the water feed was cut off, xenon slowly replaced water again.

The MAS NMR spectra showed two peaks of adsorbed xenon in hydrated ZSM-22, indicating that according to previous studies, water tends to remain at the windows of the zeolite.[95,96] This leaves space for xenon in the pockets, which remains there even after full hydration. Xenon was completely expelled from MCM-41 containing small mesopores, indicating a complete filling of the pores with water. In SBA-15 containing larger mesopores, the adsorption of water on the pore walls only reduced the apparent pore size, in line with previous results from the group of Buntkowsky, indicating that the water layer in SBA-15 grows radially toward the pore center.[97]

Ordered mesoporous silicas may be prepared by pseudomorphic transformation from controlled pore glasses (CPG). Instead of powdered samples, particles reflecting the macroscopic shape of the starting material are obtained.[98] For this process, two different mechanisms are possible: The transformation may proceed homogeneously from the outside to the inside of the particle or vice versa, or it may start in certain domains dispersed over the particle, and then spread. Matysik and co-workers tried to answer this question for the transformation of a silica gel, LiChrospher, which possesses a broad pore size distribution between 10 and 50 nm, to the well-ordered MCM-41 exhibiting hexagonally arranged pores with a very narrow pore size distribution of ≈4 nm.[99] They detected a ^{129}Xe signal with a chemical shift characteristic for the starting LiChrospher pore system throughout the reaction, until a conversion of ≈50% to MCM-41 is reached. These observations support the domain model. If, in the contrasting case, MCM-41 started to form exclusively on the outside of the particles, the LiChrospher pore system would be blocked much sooner for xenon gas. These findings were supported by a cavitation effect visible in the nitrogen physisorption isotherms of the partially transformed samples, indicating that the pore entrance of some of the starting pores is blocked by smaller pores. In a second step, the authors studied the transformation of a CPG, containing larger mesopores (around 53 nm in diameter), into MCM-41. This transformation allowed for a better spectral separation of the xenon signals inside the pores. A series of 1D EXSY spectra was recorded on a partially transformed sample. Even at short exchange times, xenon exclusively adsorbed in MCM-41 pores, and no signal characteristic for ^{129}Xe in the larger CPG pores was observed. Here, the authors conclude that MCM-41 forms at the outer surface of the particles, thus blocking the access to the remaining CPG pores at the inside, or at least slowing down the diffusion into these domains, until ^{129}Xe relaxation has destroyed the signal. The different mechanisms observed for the two systems (silica gel vs CPG) might be explained by the different pore sizes of the starting materials and thus the ability to accommodate the newly formed MCM-41 phase.

Hollow silica spheres are useful thermal isolation materials. Senker, Retsch, and co-workers investigated the porosity of such spheres with a diameter of about 316 nm and a shell thickness of 44 nm. They found two types of micropores with sizes of 0.7 and 1.1 nm, respectively, which gradually disappeared upon calcination at increasing temperatures due to sintering of the silica.[100] ^{129}Xe NMR was also successfully employed to elucidate the mesoporous structure of silica nanoparticles with a particular elongated shape, possessing hexagonally arranged, uniform mesopores, before and after decoration with silver nanoparticles.[101] ^{129}Xe NMR in combination with argon physisorption experiments allowed to determine pore sizes in new layered silica materials with organic pillars.[102] In these materials, a fascinating pore opening effect upon CO_2 adsorption was observed and explained by rotational freedom of the linkers and immobilization of this rotation by higher gas pressures.

4.3. Metal–Organic Frameworks

MOFs have attracted tremendous research interest in the last two decades due to their exceptionally high porosity and structural variability. Various possible applications in catalysis, sensing, and gas separation and adsorption have been proposed. While their crystalline structure is accessible by X-ray diffraction, many other structural features such as disordered side chains, dynamic linker behavior, and adsorption processes are invisible in XRD. In contrast, solid-state NMR is sensitive for short range interactions and dynamic effects. MOFs exhibit well-defined pore sizes and a well-tunable surface chemistry.^{129}Xe NMR is particularly sensitive toward these parameters and thus ideally suited to study these materials. By recording the chemical shift of xenon confined in MOFs in variable pressure experiments, "chemical shift isotherms" can be obtained, comparable to other gas physisorption isotherms. These allow in particular to follow the peculiar behavior of guest-induced crystal structure transitions in MOFs, the so-called breathing effect.[65,78,103]

The sorption properties of MOFs can be modified by introducing linker modifications or side chains, rendering the materials interesting candidates for gas separation or sensing applications. Side chains however also introduce disorder. Kemnitzer et al. investigated this disorder effect in the MOF CAU-1, where one out of the four free positions at the aromatic linkers was modified with amino, acetamide, and methyl urea side chains.[104] The chemical shifts of adsorbed xenon calculated by the Fraissard approach were not expected to be suitable here due to the influence of the charged metal nodes. Existing DFT kernels for determining pore dimensions and linker distribution using argon physisorption were also found unsuitable. The authors thus optimized the MOF structures in DFT calculations (**Figure 6**a) and calculated the chemical shifts for xenon adsorbed in many different positions in the structure, yielding an average ^{129}Xe shift. These calculated values were compared to the so-called limiting shift values at high temperature, where Xe–Xe interactions can be neglected and Xe–wall interactions dominate (Figure 6b). The different modifications allowed to

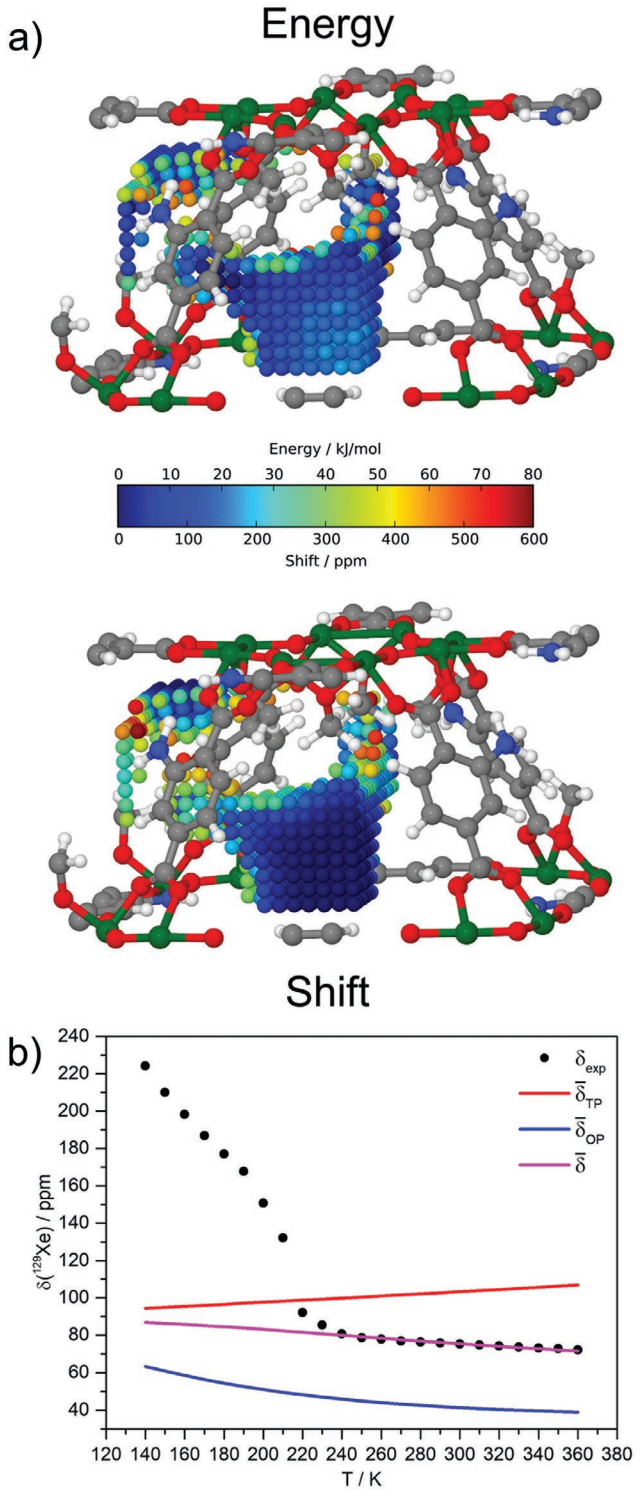

Figure 6. a) Grid of xenon positions within the selected fraction of the unit cell. Energy (top) and ^{129}Xe isotropic chemical shift (bottom) are color coded with the color bar shown below. For a better overview, only half of the unit cell is shown. White: hydrogen, grey: carbon, red: oxygen, blue: nitrogen, green: aluminum. b) Experimental (δ_{exp}) and theoretical ($\bar{\delta}$) values of the isotropic ^{129}Xe chemical shift for each measured temperature. Averaged contributions of the octahedral ($\bar{\delta}_{OP}$) and tetrahedral ($\bar{\delta}_{TP}$) are shown. Isotropic shifts were corrected with a constant value of 41.5 ppm to match the experimental data. Reproduced with permission.[104] Copyright 2018, American Chemical Society.

calibrate the increase in ^{129}Xe chemical shift with decreasing pore size. Side chains were found to point preferentially into the larger octahedral voids. The developed model is expected to be applicable also for other MOFs for determining the orientation of disordered side chains and for the estimation of pore sizes.

A DFT model for predicting the chemical shifts of xenon in the high pressure limit in UiO-66 and UiO-67 was developed by Seifert, Brunner, and co-workers.[105] It takes into account xenon–xenon pair and xenon–wall interactions, combined with MD simulations for equilibrating the distribution of xenon atoms in the different pore types. The calculated chemical shifts agreed well with the experimental data, also in the high pressure range up to 17 bar. The DFT model is expected to be applicable for larger UiO-type materials. However, at pressures above 1 bar, a more complex correlation was observed between the ^{129}Xe chemical shift and the volumetric xenon uptake, explained by the fact that xenon–xenon interactions may become more complex in the limit of high gas density.[106]

^{129}Xe NMR was also used to study the breathing behavior of the flexible MOF Al-MIL-53. With xenon as guest phase, a slow phase transition is induced by temperature increase between 240 and 330 K, which the authors could follow by the signal intensities of xenon in the narrow pore and the open pore form of the MOF.[107] In a mixed-phase stage of the MOF, they carried out one of the rare ^{1}H-^{129}Xe cross polarization experiments under MAS (**Figure 7**), and could only observe signals of the narrow pore form, which they explain by the lower mobility of the gas in these pores. They also determined the exchange rate between the two pores by selective inversion recovery spectra.

If the synthesis of Al-MIL-53 is performed in acetonitrile, differing from the standard synthesis, a rigid large pore form of Al-MIL-53 is obtained, that does not show the usual breathing effect upon water adsorption.[108] To investigate whether or not a hydrophobic guest molecule may reintroduce this flexibility, VT

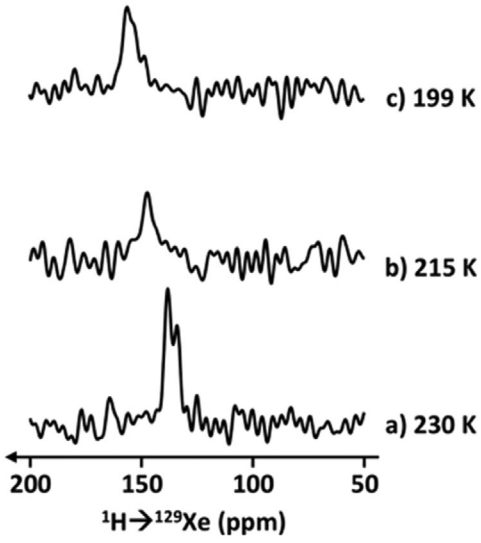

Figure 7. 1D ^{1}H-^{129}Xe CPMAS spectra of the np form of the MIL-53(Al) loaded with xenon and recorded at ν_R = 8 kHz and a) 230 K, b) 215 K, and c) 199 K. Reproduced with permission.[107] Copyright 2017, American Chemical Society.

^{129}Xe NMR spectra were recorded between 295 and 140 K. No signals of the MIL-53 narrow pore form were observed, thus, the breathing effect was not active in MIL-53 produced by this route. Interestingly, between 260 and 190 K several signals were observed which were attributed to different clusters of adsorbed Xe, in line with results from Brunner, Volkmer, and co-workers.[109] A significant number of defects as a consequence of the small particle size[110] may be the reason for the stabilization of the MOF and the inhibition of the breathing behavior.

^{129}Xe has also been demonstrated to be an important tool to locate metal nanoparticles in MOFs. The localization of metal nanoparticles in MOFs, either embedded in the pore system, encapsulated by the MOF, or decorating the outer surface of the MOF, has been so far a great challenge, but has a huge impact on the catalytic performance. By 3D scanning transmission electron microscope tomography, Jiang and co-workers found a homogeneous distribution of either Pt and Pt_1Cu_2 nanoparticles embedded in MIL-101.[111] The authors investigated MOF samples with varying metal particle loading with ^{129}Xe NMR and observed increasing ^{129}Xe chemical shifts with growing NP loadings. A homogenous distribution of the nanoparticles inside the pore system could be shown.

The effect of electron-withdrawing groups was impressively demonstrated by Lima and co-workers exploiting the high xenon polarizability.[112] Investigating a mixed linker MIL-101(Cr) containing terephthalic acid and only 1% tetrafluoroterephthalic acid, they found a chemical shift of xenon adsorbed in the pores shifting downfield by 38 ppm, clearly evidencing the incorporation of the fluorinated linker. In addition, the paramagnetic Cr^{III} centers were found to induce a paramagnetic shift not only to the adsorbed Xe, but also a shift of 10–20 ppm to gas phase xenon in inter-particle voids.

The groups of Kaskel and Brunner recently reported that DUT-49 exhibits a sudden desorption of methane and xenon above a certain pressure, an effect that the authors dubbed negative gas adsorption.[113,114] The effect is explained by an energetically favorable state in the closed pore form in a certain range of guest molecules per pore.[115] The authors investigated the effect of lattice defects on the breathing behavior by ^{129}Xe NMR. A series of samples with different crystal sizes and different percentages of lattice defects, by partial replacement of the linker with a similar molecule, was synthesized. ^{129}Xe was used as a sensitive probe for the structure contraction, indicated by a sudden low field shift. In addition, for smaller crystals, lower ^{129}Xe chemical shifts were observed. While crystal size did not perturb the phase transformation, a high concentration of crystal lattice defects did inhibit the structure contraction. ^{129}Xe NMR spectroscopic investigation of a series of DUT-49-type MOFs with linkers of different lengths allowed the authors to deduce a correlation between ^{129}Xe chemical shifts and the pore size, allowing to estimate pore volumes in similar materials. The structural contraction was also observed in DUT-50 with an even longer linker than DUT-49, while shorter linkers yielded materials without structural flexibility.[116]

HP xenon entrapped in ZIF-8 crystallites in aqueous solution has recently been shown to increase the hyperpolarized signal intensity by a factor of four compared to xenon dissolved in water.[117] The authors compare this entrapment of xenon in a MOF to xenon in molecular cages such as cryptophane-A, used in medical imaging for specific binding to certain biomolecules.[118,119] As the xenon signal intensity in such cages is often very low, HP xenon-ZIF signals were found to be 200 times higher than those of the xenon-cryptophane-A complex. Further studies may shed light on the origins of this effect and indicate a route toward medical applications as predicted by the authors.

Berens et al. studied the self-diffusion of several gases, including xenon, in pristine ZIF-8 and hybrid ZIF-7-8, containing two different linkers, with PFG NMR.[120] The intracrystalline self-diffusion was lower in ZIF-7-8 due to its smaller pore opening. For ethane and larger gas molecules, no difference in diffusion selectivity was however observed, suggesting some network flexibility for both ZIF materials.

The dynamic behavior of polymers and coordination polymers is not accessible by X-ray diffraction, but it is accessible by ^{129}Xe NMR. The group of Wang probed the dynamics of an interpenetrated covalent organic framework.[121] In both static pressure and variable temperature and constant temperature and variable pressure experiments, the reversible phase transition from the closed to the open pore form was followed. The phase transition occurred gradually, highlighted by the presence of two distinctive xenon signals.

4.4. Miscellaneous Materials

Small organic cages are known to capture xenon, giving rise to high chemical shifts and anisotropic signals due to the strong confinement.[13] They may serve as possible separation materials for noble gases.[122–124] They are also promising as biosensors in medical magnetic resonance imaging, delivering HP xenon to the tissue, including the possibility to attach functional groups for specific binding to the cage.[125] The crystalline material investigated by Telkki and co-workers forms an interconnected 3D pore structure with cavities (cages), cage windows, and channels connecting the cages with a diameter of 0.44 nm, which is just above the atomic diameter of xenon (0.41 nm).[126] The pore channels are only 0.36 nm in diameter, however, their flexibility allows for xenon diffusion. Using density functional theory, the authors developed a two-site exchange model that allowed to calculate the population of both cavities and window cages in the fast exchange regime by measuring the averaged chemical shift. From the longitudinal relaxation times of xenon at different loadings, the exchange rates between the sites were determined. Using chemical exchange saturation transfer (CEST) experiments, probing the exchange of mobile protons, they found indications for the presence of even more sites. This lead to a four-site model, including cage cavities, the window cavities, window cavities in which xenon is stuck and the free gas around the crystalline particles. The same group further studied the relaxation parameters of both xenon and sulfur hexafluoride SF_6, a potent greenhouse gas, by combining the developed DFT models with experiments.[122] They elucidated T_1 and T_2 relaxation mechanisms and the different dynamics of the two gases in an organic cage (CC3-R).

Strong confinement effects of xenon were also observed in crystalline 1D *bis*-urea nano-channels.[20,21] In a macrocycle with small channels sized $\approx 0.4 \times 0.4$ nm^2, absorbed xenon showed a pronounced chemical shift anisotropy, evidencing the strong

distortion of electron density of adsorbed xenon due to the confinement. Single-file diffusion of xenon through the channels was observed. In contrast, xenon adsorbed in a macrocycle with larger channels sized 0.9 × 0.9 nm^2, an isotropic ^{129}Xe NMR signal, lower deshielding, and normal Fickian diffusion were found.

Weller and co-workers investigated the behavior of nonporous solid-state molecular organic frameworks that undergo a single-crystal to single-crystal transformation upon exposure to a guest molecule such as dichloromethane.[127] Upon evacuation, CH_2Cl_2 was released from the structure without any significant structural change and a large hydrophobic cavity was formed. After exposure to xenon, 1D ^{129}Xe NMR spectra at 298 K showed a broad signal at 185 ppm of adsorbed xenon in addition to the gas phase peak. No correlation in EXSY spectra between the signals was observed for contact times up to 1.2 s, indicating no significant exchange with the gas phase.

The advantage of ^{129}Xe NMR in crystal structure determination of porous materials which are not suitable for (powder) X-ray diffraction analysis was further demonstrated by the group of Lantto.[128] They used experimental and computational ^{129}Xe NMR isotropic chemical shifts and chemical shift anisotropies to elucidate the structure of two new fluorophenol clathrates.

Finally, ^{129}Xe NMR was used to estimate the pore size in mixed matrix materials consisting of polymers of intrinsic microporosity as matrix and agglomerates of silica nanoparticles as fillers.[129] The deconvolution of 1D ^{129}Xe NMR spectra allowed the authors to differentiate the contributions of the matrix and of the filler.

Silicon is considered as inexpensive and high capacity anode material for lithium intercalation in lithium batteries. Silicon however undergoes significant volume expansion and restructuration during the intercalation. Silicon sponges reported by Wang and co-workers are presented as an alternative with strongly reduced volume expansion.[130] The authors studied four different materials with varying pore and particle sizes. ^{129}Xe NMR line width analysis indicated different pore size distribution of the micropores in the different materials. Based on their findings, the authors established a model of mesoporous channels with branching micropores. In the following, the group studied a mesoporous silicon sponge material modified with C_{18} alkyl chains.[131] The authors found a blocking of the micropores by the alkyl chains, leading to the disappearance of strong xenon adsorption sites.

Carbon nanotubes represent a further possible electrode material, but they are also interesting for many other electronic applications due to their tunability and controllable properties. Using an in situ HP ^{129}Xe NMR flow set-up, Bao and co-workers studied the adsorption and desorption of methanol during competitive adsorption of xenon in single-walled carbon nanotubes (SWNT) and in MCM-41.[132] The authors first adsorbed xenon on MCM-41 and then added a methanol flow, which replaced xenon at the silica surface. The xenon signal intensity over time decreased at a faster rate in the beginning, followed by a distinctly slower rate. The authors explained these two steps by first, initial single molecule adsorption to silanol groups and second, the formation of methanol multi-layer aggregates and adsorption of gas molecules to this layer. The methanol flow was then switched off and methanol was slowly replaced by xenon adsorption. Again first a faster desorption of methanol from the aggregate occurred, followed by slower desorption of single molecules bound to the silica. In contrast, in SWNT, xenon inside the nanotubes was replaced by methanol in a much faster one-step process. Additionally, a reduction of the xenon signal intensities was observed, that the authors attributed to depolarization of the hyperpolarized xenon by the non-localized electrons in the carbon nanotubes.

Natural materials are often characterized by their complex composition, which may vary strongly as a function of their origin. Low-cost natural materials such as rocks, minerals, or biogenic waste materials, are often used in large-scale industrial applications. Therefore, straightforward, non-destructive tools are required for their unambiguous analysis. Recent examples show that ^{129}Xe NMR is a useful tool to determine the porosity of complex materials, allowing to link the material's origin to its properties and give insights into their composition.

Content and composition of organic matter in rocks are important factors for the formation of natural oil and gas. The two sources of organic matter are bitumen, soluble in organic solvents, and insoluble kerogen. The ratio of hydrogen, carbon, and oxygen and the ratio between aromatic and aliphatic components in kerogen determines its ability to transform into natural oil. The use of solid-state NMR was investigated by Clough et al. as a non-destructive technique to directly assess the organic matter inside the source rock.[133] The authors successfully determined the composition of several kerogen, bitumen and source rock samples with ^{1}H, ^{13}C direct excitation, and ^{13}C cross polarization solid-state NMR under MAS. With ^{129}Xe NMR using the Fraissard approach,[24] the authors were able to correlate the decreasing size of mesopores with increasing thermal maturity of the samples, thus introducing ^{129}Xe NMR as a straightforward, non-destructive tool.

In cement materials, the pore network determines their strength and durability. Therefore, ^{129}Xe NMR was used successfully to determine pore sizes and diffusion between the free gas and mesopores in hydrated cements from different manufactures.[134] In the same work, the authors also studied shale sample of different origins, in which the pore network is crucial for diffusion of natural gas. By ^{129}Xe spin–echo spectra, they found micropores and mesopores with the pore sizes ranging from 1 to 10 nm. In shale samples from China, the authors observed very broad ^{129}Xe resonances with negative chemical shifts down to –400 ppm, indicative for the presence of paramagnetic impurities. They attributed this effect to a significant amount of Fe^{II}-containing siderite in the material. Shale samples from United States also contain an Fe^{II} impurity, pyrite, in which the Fe^{II} centers are present in low-spin configuration. Therefore, no paramagnetic effect on ^{129}Xe was observed in this material. Thus, the authors demonstrate how ^{129}Xe may be useful to sensitively track paramagnetic impurities even in complex samples.

Biogenic silica is produced by unicellular diatoms in the shape of intricately structured cell walls. Sedimented and fossilized diatom biosilica, so-called diatomaceous earth, is a low-cost raw material and finds numerous applications as filter material, abrasive or desiccant. Puente-Urbina et al. methylated purified diatomaceous earth.[135] As expected from this very heterogeneous natural material, HP ^{129}Xe NMR indicated

a large pore size distribution. The authors found signals characteristic for xenon gas inside methylated pores, but their low intensity indicated incomplete methylation. Concluding from 2D EXSY spectra, the authors hypothesized that the methylated pores were not accessible from the free gas space, but only from non-methylated pores containing SiOH groups.

A porous low-cost natural material is also obtained by carbonization of almond shells, and represents a possible resource for purification applications or composite fillers.[136] The thermal treatment yielded mesopores beside large macropores, assessed by ^{129}Xe NMR and nitrogen physisorption. Washing of the samples removed soot and salts and opened up micropores, accessible for ^{129}Xe from the gas phase as evidenced by 2D EXSY spectra.

4.5. ^{129}Xe NMR in In Situ Set-Ups for Catalysis and Combination with PHIP

The group of Koptyug has implemented nuclear magnetic imaging in a catalytic reactor, using hyperpolarized hydrogen gas as reactant for hydrogenation reactions, thus strongly increasing the signal intensity. In the reactor, the group was able to monitor, on a scale of several millimeters, the distribution of products and educts online during catalysis, thus obtaining information about reaction zones and flow profiles inside the reactor.[137,138] Into the reactant gas flow, they added hyperpolarized xenon, using the well-known temperature dependence of the chemical shift of ^{129}Xe to calibrate the temperature inside an in situ reaction chamber.[139] HP xenon gas thus proved to be a more accurate temperature probe than an external thermocouple. Using this set-up, they studied the hydrogenation of propene in a H_2 gas flow, with Pt nanoparticles deposited on alumina as catalyst. ^{1}H magnetic resonance imaging of the reaction cell indicated 100% conversion where H_2 was in contact with the catalyst.

The group of Bao has developed an in situ continuous flow xenon adsorption set-up in which HP xenon can be mixed with another adsorbate gas prior to contacting the mixture with a porous material. Either gas can be switched on and off at certain points in order to follow the response of the system. The set-up allows for the online detection of adsorption processes, in particular for competitive adsorption of xenon gas against water or reactant gases such as methanol. Time-resolved ^{129}Xe NMR spectra and ^{1}H NMR spectra can be recorded during the adsorption, also alternating experiments with different nuclei are feasible. Several studies carried out with this set-up on different materials have been described in Sections 4.1.1 and 4.4.[86,88,132]

Ionic liquids (IL) have gained increasing interest in the last years due to their high application potential as non-volatile solvents with low toxicity.[140] They cannot be described as strictly porous materials, but they may form voids which accommodate xenon atoms. The group of Mele has shown how the chemical shift of xenon is influenced by the space of the void and the charge of the surrounding IL.[141] The chemical shift of ^{129}Xe dissolved in bulk IL also sensitively reacts to the nature of the ions such as different halide ions and the alkyl chain lengths of imidazolium cations,[142,143] and it shows a dependence on the mixing volume of an IL mixture.[144,145] The group also assessed the diffusion of xenon in different IL in order to better understand separation processes in IL phases.[146] Heinze et al. also used ^{129}Xe NMR along with nitrogen physisorption to evaluate the behavior of IL in porous silica supports such as SBA-15 and MCM-41. Particular emphasis was placed on studying the formation of isolated droplets versus layers.[147]

5. Conclusions

^{129}Xe NMR has developed in the past decades into a powerful tool to study the porous structure of functional materials. Pore sizes can be precisely determined by ^{129}Xe NMR, provided that a suitable model for similar materials is present. If this is not the case, it is favorable to establish an empirical correlation, for example, on homologous series of similar materials with different pore sizes. The works discussed in Section 2.3 and recent works have shown that in general, pore sizes determined by ^{129}Xe NMR correspond well to the pore sizes established by other techniques such as nitrogen physisorption. Pore connectivity or pore blocking can be clearly made visible by ^{129}Xe 2D EXSY, and the time scale of chemical exchange between two environments can be calculated or at least estimated. These parameters are particularly important for demonstrating hierarchy in modern materials. It has been demonstrated that true hierarchy can be made visible in EXSY spectra by a series of different xenon signals, interconnected by cross peaks. For these materials with complex porous structures, it is desirable to combine results from ^{129}Xe spectra with gas adsorption techniques, which have shown an increasing potential in recent years and which now allow to determine pore sizes and to visualize pore geometry effects such as cavitation.[148]

^{129}Xe spectra thus allow to obtain insights into many material properties, in particular the surface chemistry of the pore walls, structural dynamics and flexibility. Ultimately, this allows to better understand the function of the materials under study, such as their adsorption properties and catalytic activity. Due to its versatility, ^{129}Xe NMR will continue to be extended to new classes of materials. In future, it could also be extended to probing infiltrated phases in porous materials, as demonstrated for ammonia borane[149] or ibuprofen[150] in mesoporous silica.

With regard to the investigation of hierarchical materials, the combination of ^{129}Xe NMR spectroscopy with the increasing power of molecular dynamic approaches will allow to develop better models of the confinement of xenon in complex pore systems. In particular, from EXSY exchange rates, an estimation of xenon mean free paths and geometric models of a pore network, namely the actual mean distances between pores of different sizes may become accessible, leading to an overall textural model of the materials. Diffusion restriction by narrow pore openings may also be included in these considerations. In situ set-ups allowing for co-adsorption of xenon with other gases such as the one developed by the group of Bao may prove particularly useful to study adsorption processes and catalytic activity in functional hierarchical materials. Finally, the use of ^{129}Xe NMR for the investigation of supported ionic liquid catalysts (SILP) may gain importance as this new class of materials is increasingly used in catalysis.

While the inherently low sensitivity of NMR can be compensated by xenon hyperpolarization, this still requires a dedicated set-up. The advent of an increasing number of dissolution DNP polarizers might one day present an alternative way to hyperpolarize xenon, if higher amounts of HP xenon can be produced in shorter time. Coupling with adapted probes for the investigation of materials is then also thinkable.

Acknowledgements

Generous financial support of the work in this area by Bayerisch-Tschechische Hochschulagentur (BTHA) is gratefully acknowledged. The authors thank Stephan Glante for the careful proof-reading of the manuscript.

Open access funding enabled and organized by Projekt DEAL.

Conflict of Interest

The authors declare no conflict of interest.

Keywords

hierarchical materials, nuclear magnetic resonance, porosity, xenon

Received: July 16, 2020
Revised: August 21, 2020
Published online:

[1] J. Fraissard, *eMagRes* **2007**, https://doi.org/10.1002/9780470034590.emrstm0311.
[2] P. J. Barrie, J. Klinowski, *Prog. Nucl. Magn. Reson. Spectrosc.* **1992**, *24*, 91.
[3] C. Dybowski, N. Bansal, T. M. Duncan, *Annu. Rev. Phys. Chem.* **1991**, *42*, 433.
[4] T. Ito, J. Fraissard, in *Proc. 5th Int. Conf. on Zeolites* (Ed: L. V. C. Rees) **1980**, pp. 510–515.
[5] J. A. Ripmeester, D. W. Davidson, *J. Mol. Struct.* **1981**, *75*, 67.
[6] M. Hartmann, A. G. Machoke, W. Schwieger, *Chem. Soc. Rev.* **2016**, *45*, 3313.
[7] K. J. D. MacKenzie, M. E. Smith, *Multinuclear Solid-State Nuclear Magnetic Resonance of Inorganic Materials*, Vol. *6*, Pergamon, Oxford **2002**.
[8] M. Duer, (Ed), *Introduction to Solid-State NMR Spectroscopy*, Wiley-Blackwell, Hoboken, NJ **2004**.
[9] D. Engelhard, G. Michel, *High-Resolution Solid-State NMR of Silicates and Zeolites*, John Wiley & Sons, Ltd, Hoboken, NJ **1986**.
[10] C. J. Jameson, A. K. Jameson, S. M. Cohen, *J. Chem. Phys.* **1973**, *59*, 4540.
[11] T. Ito, J. Fraissard, *Zeolites* **1988**, *8*, 350.
[12] T. Ito, J. Fraissard, *J. Chem. Phys.* **1982**, *76*, 5225.
[13] C. J. Jameson, in *Hyperpolarized Xenon-129 Magnetic Resonance: Concepts, Production, Techniques and Applications* (Eds: T. Meersmann, E. Brunner), The Royal Society of Chemistry, London **2015**, pp. 16–48.
[14] T. T. P. Cheung, *J. Phys. Chem.* **1995**, *99*, 7089.
[15] L.-C. de Ménorval, J. P. Fraissard, T. Ito, *J. Chem. Soc., Faraday Trans. 1* **1982**, *78*, 403.
[16] T. Ito, J. Fraissard, *J. Chem. Soc., Faraday Trans. 1* **1987**, *83*, 451.
[17] J. Kritzenberger, H. C. Gaede, J. S. Shore, A. Pines, A. T. Bell, *J. Phys. Chem.* **1994**, *98*, 10173.
[18] M. Hartmann, B. Boddenberg, *Microporous Mater.* **1994**, *2*, 127.
[19] Q. Cao, N. Andrijchenko, A. Ermilov, M. Räsänen, A. Nemukhin, L. Khriachtchev, *J. Phys. Chem. A* **2015**, *119*, 2587.
[20] C. R. Bowers, M. Dvoyashkin, S. R. Salpage, C. Akel, H. Bhase, M. F. Geer, L. S. Shimizu, *ACS Nano* **2015**, *9*, 6343.
[21] C. R. Bowers, M. Dvoyashkin, S. R. Salpage, C. Akel, H. Bhase, M. F. Geer, L. S. Shimizu, *Can. J. Chem.* **2015**, *93*, 1031.
[22] V. V. Terskikh, I. L. Moudrakovski, V. M. Mastikhin, *J. Chem. Soc., Faraday Trans.* **1993**, *89*, 4239.
[23] V. V. Terskikh, I. L. Moudrakovski, S. R. Breeze, S. Lang, C. I. Ratcliffe, J. A. Ripmeester, A. Sayari, *Langmuir* **2002**, *18*, 5653.
[24] J. Demarquay, J. Fraissard, *Chem. Phys. Lett.* **1987**, *136*, 314.
[25] F. Cros, J. P. Korb, L. Malier, *Langmuir* **2000**, *16*, 10193.
[26] S. Hamoudi, Y. Yang, I. L. Moudrakovski, S. Lang, A. Sayari, *J. Phys. Chem. B* **2001**, *105*, 9118.
[27] T. Meersmann, J. W. Logan, R. Simonutti, S. Caldarelli, A. Comotti, P. Sozzani, L. G. Kaiser, A. Pines, *J. Phys. Chem. A* **2000**, *104*, 11665.
[28] F. Chen, C. L. Chen, S. Ding, Y. Yue, C. Ye, F. Deng, *Chem. Phys. Lett.* **2004**, *383*, 309.
[29] A. Julbe, L. C. De Ménorval, C. Balzer, P. David, J. Palmeri, C. Guizard, *J. Porous Mater.* **1999**, *6*, 41.
[30] K. V. Romanenko, X. Py, J. B. D'Espinose De Lacaillerie, O. B. Lapina, J. Fraissard, *J. Phys. Chem. B* **2006**, *110*, 3055.
[31] K. V. Romanenko, O. B. Lapina, X. Py, J. Fraissard, *Russ. J. Gen. Chem.* **2008**, *78*, 2171.
[32] K. V. Romanenko, J. B. d'Espinose de Lacaillerie, O. Lapina, J. Fraissard, *Microporous Mesoporous Mater.* **2007**, *105*, 118.
[33] B. Driehuys, G. D. Cates, E. Miron, K. Sauer, D. K. Walter, W. Happer, *Appl. Phys. Lett.* **1996**, *69*, 1668.
[34] T. G. Walker, W. Happer, *Rev. Mod. Phys.* **1997**, *69*, 629.
[35] G. Norquay, G. J. Collier, M. Rao, N. J. Stewart, J. M. Wild, *Phys. Rev. Lett.* **2018**, *121*, 153201.
[36] E. Weiland, M. A. Springuel-Huet, A. Nossov, A. Gédéon, *Microporous Mesoporous Mater.* **2016**, *225*, 41.
[37] T. Meersmann, G. Pavlovskaya, in *Hyperpolarized Xenon-129 Magnetic Resonance: Concepts, Production, Techniques and Applications* (Eds: T. Meersmann, E. Brunner), The Royal Society of Chemistry, London **2015**, pp. 49–71.
[38] H. J. Jänsch, P. Gerhard, M. Koch, *Proc. Natl. Acad. Sci. USA* **2004**, *101*, 13715.
[39] M. Haake, A. Pines, J. A. Reimer, R. Seydoux, *J. Am. Chem. Soc.* **1997**, *119*, 11711.
[40] E. Brunner, R. Seydoux, M. Haake, A. Pines, J. A. Reimer, *J. Magn. Reson.* **1998**, *130*, 145.
[41] E. V. Krjukov, J. D. O'Neill, J. R. Owers-Bradley, *J. Low Temp. Phys.* **2005**, *140*, 397.
[42] A. Honig, X. Wei, A. Lewis, E. ter Haar, K. Seraji-Bozorgzad, *Phys. B Condens. Matter* **2000**, *284-288*, 2049.
[43] A. Capozzi, C. Roussel, A. Comment, J. N. Hyacinthe, *J. Phys. Chem. C* **2015**, *119*, 5020.
[44] N. N. Kuzma, M. Pourfathi, H. Kara, P. Manasseh, R. K. Ghosh, J. H. Ardenkjaer-Larsen, S. J. Kadlecek, R. R. Rizi, *J. Chem. Phys.* **2012**, *137*, 104508.
[45] A. Comment, S. Jannin, J.-N. Hyacinthe, P. Miéville, R. Sarkar, P. Ahuja, P. R. Vasos, X. Montet, F. Lazeyras, J.-P. Vallée, P. Hautle, J. A. Konter, B. van den Brandt, J.-P. Ansermet, R. Gruetter, G. Bodenhausen, *Phys. Rev. Lett.* **2010**, *105*, 018104.
[46] P. Sozzani, S. Bracco, A. Comotti, in *Hyperpolarized Xenon-129 Magnetic Resonance: Concepts, Production, Techniques and Applications* (Eds.: T. Meersmann, E. Brunner), The Royal Society of Chemistry, London **2015**, pp. 164–184.
[47] J. E. Roos, H. P. McAdams, S. S. Kaushik, B. Driehuys, *Magn. Reson. Imag. Clin. N. Am.* **2015**, *23*, 217.
[48] J. P. Mugler, T. A. Altes, *J. Magn. Reson. Imaging* **2013**, *37*, 313.

[49] R. G. Larsen, J. Shore, K. Schmidt-Rohr, L. Emsley, H. Long, A. Pines, M. Janicke, B. F. Chmelka, *Chem. Phys. Lett.* **1993**, *214*, 220.
[50] I. L. Moudrakovski, C. I. Ratcliffe, J. A. Ripmeester, *J. Am. Chem. Soc.* **1998**, *120*, 3123.
[51] L. Q. Wang, in *Hyperpolarized Xenon-129 Magnetic Resonance: Concepts, Production, Techniques and Applications* (Eds: T. Meersmann, E. Brunner), The Royal Society of Chemistry, London **2015**, pp. 142–163.
[52] Y. Liu, W. Zhang, Z. Liu, S. Xu, Y. Wang, Z. Xie, X. Han, X. Bao, *J. Phys. Chem. C* **2008**, *112*, 15375.
[53] W. Schwieger, A. G. Machoke, T. Weissenberger, A. Inayat, T. Selvam, M. Klumpp, A. Inayat, *Chem. Soc. Rev.* **2016**, *45*, 3353.
[54] D. Zhao, J. Feng, Q. Huo, N. Melosh, G. H. Fredrickson, B. F. Chmelka, G. D. Stucky, *Science* **1998**, *279*, 548.
[55] F. Hoffmann, M. Cornelius, J. Morell, M. Fröba, *Angew. Chem., Int. Ed.* **2006**, *45*, 3216.
[56] A. Silvestre-Albero, E. O. Jardim, E. Bruijn, V. Meynen, P. Cool, A. Sepúlveda-Escribano, J. Silvestre-Albero, F. Rodríguez-Reinoso, *Langmuir* **2009**, *25*, 939.
[57] A. Silvestre-Albero, M. Gonalves, T. Itoh, K. Kaneko, M. Endo, M. Thommes, F. Rodríguez-Reinoso, J. Silvestre-Albero, *Carbon* **2012**, *50*, 66.
[58] R. W. Mair, G. P. Wong, D. Hoffmann, M. D. Hürlimann, S. Patz, L. M. Schwartz, R. L. Walsworth, *Phys. Rev. Lett.* **1999**, *83*, 3324.
[59] V. V. Telkki, J. Lounila, J. Jokisaari, in *Hyperpolarized Xenon-129 Magnetic Resonance: Concepts, Production, Techniques and Applications* (Eds: T. Meersmann, E. Brunner), The Royal Society of Chemistry, London **2015**, pp. 185–199.
[60] T. Onfroy, F. Guenneau, M. A. Springuel-Huet, A. Gédéon, *Carbon* **2009**, *47*, 2352.
[61] M. Oschatz, H. C. Hoffmann, J. Pallmann, J. Schaber, L. Borchardt, W. Nickel, I. Senkovska, S. Rico-Francés, J. Silvestre-Albero, S. Kaskel, E. Brunner, *Chem. Mater.* **2014**, *26*, 3280.
[62] R. Ryoo, C. H. Ko, M. Kruk, V. Antochshuk, M. Jaroniec, *J. Phys. Chem. B* **2000**, *104*, 11465.
[63] M. Hartmann, A. Vinu, *Langmuir* **2002**, *18*, 8010.
[64] A. Nossov, E. Haddad, F. Guenneau, A. Galarneau, F. Di Renzo, F. Fajula, A. Gédéon, *J. Phys. Chem. B* **2003**, *107*, 12456.
[65] H. C. Hoffmann, B. Assfour, F. Epperlein, N. Klein, S. Paasch, I. Senkovska, S. Kaskel, G. Seifert, E. Brunner, *J. Am. Chem. Soc.* **2011**, *133*, 8681.
[66] M.-A. Springuel-Huet, A. Nossov, F. Guenneau, A. Gédéon, *Chem. Commun.* **2013**, *49*, 7403.
[67] A. G. Slater, A. I. Cooper, *Science* **2015**, *348*, aaa8075.
[68] N. Chaoui, M. Trunk, R. Dawson, J. Schmidt, A. Thomas, *Chem. Soc. Rev.* **2017**, *46*, 3302.
[69] I. L. Moudrakovski, C. I. Ratcliffe, J. A. Ripmeester, L.-Q. Wang, G. J. Exarhos, T. F. Baumann, J. H. Satcher, *J. Phys. Chem. B* **2005**, *109*, 11215.
[70] K. J. Ooms, K. Campbell, R. R. Tykwinski, R. E. Wasylishen, *J. Mater. Chem.* **2005**, *15*, 4318.
[71] W. O. Parker, A. Ferrando, D. Ferri, V. Canepari, *Macromolecules* **2007**, *40*, 5787.
[72] D. R. Morgan, E. O. Stejskal, A. L. Andrady, *Macromolecules* **1999**, *32*, 1897.
[73] R. Simonutti, S. Bracco, A. Comotti, M. Mauri, P. Sozzani, *Chem. Mater.* **2006**, *18*, 4651.
[74] L. Q. Wang, D. Wang, J. Liu, G. J. Exarhos, S. Pawsey, I. Moudrakovski, *J. Phys. Chem. C* **2009**, *113*, 6577.
[75] L. Q. Wang, D. Wang, J. Liu, G. J. Exarhos, *J. Phys. Chem. C* **2012**, *116*, 22.
[76] L. Q. Wang, Y. Shin, W. D. Samuels, G. J. Exarhos, I. L. Moudrakovski, V. V. Terskikh, J. A. Ripmeester, *J. Phys. Chem. B* **2003**, *107*, 13793.
[77] E. Weiland, M.-A. Springuel-Huet, A. Nossov, F. Guenneau, A.-A. Quoineaud, A. Gédéon, *New J. Chem.* **2016**, *40*, 4447.
[78] H. C. Hoffmann, E. Brunner, in *Hyperpolarized Xenon-129 Magnetic Resonance: Concepts, Production, Techniques and Applications* (Eds: T. Meersmann, E. Brunner), The Royal Society of Chemistry, London **2015**, pp. 234–248.
[79] E. Weiland, M. A. Springuel-Huet, A. Nossov, A. Gédéon, *Microporous Mesoporous Mater.* **2016**, *225*, 41.
[80] J. Fraissard, in *Hyperpolarized Xenon-129 Magnetic Resonance: Concepts, Production, Techniques and Applications* (Eds: T. Meersmann, E. Brunner), The Royal Society of Chemistry, London **2015**, pp. 1–15.
[81] S. Gao, S. Xu, Y. Wei, Z. Liu, A. Zheng, P. Wu, Z. Liu, *Chem. Commun.* **2019**, *55*, 10693.
[82] S. Xu, W. Zhang, X. Liu, X. Han, X. Bao, *J. Am. Chem. Soc.* **2009**, *131*, 13722.
[83] J.-L. Bonardet, J. Fraissard, A. Gédéon, M.-A. Springuel-Huet, *Catal. Rev.: Sci. Eng.* **1999**, *41*, 115.
[84] C. J. Jameson, A. K. Jameson, R. Gerald, A. C. de Dios, *J. Chem. Phys.* **1992**, *96*, 1676.
[85] T. He, X. Liu, S. Xu, X. Han, X. Pan, G. Hou, X. Bao, *J. Phys. Chem. C* **2016**, *120*, 22526.
[86] K. Gong, F. Jiao, Y. Chen, X. Liu, X. Pan, X. Han, X. Bao, G. Hou, *J. Phys. Chem. C* **2019**, *123*, 17368.
[87] S. Gao, S. Xu, Y. Wei, Q. Qiao, Z. Xu, X. Wu, M. Zhang, Y. He, S. Xu, Z. Liu, *J. Catal.* **2018**, *367*, 306.
[88] Z. Ji, H. Lv, X. Pan, X. Bao, *J. Catal.* **2018**, *361*, 94.
[89] Z. Qin, K. A. Cychosz, G. Melinte, H. El Siblani, J. P. Gilson, M. Thommes, C. Fernandez, S. Mintova, O. Ersen, V. Valtchev, *J. Am. Chem. Soc.* **2017**, *139*, 17273.
[90] Z. Zhao, X. Li, S. Li, S. Xu, X. Bao, Y. Bilge, P. Andrei-Nicolae, M. Ulrich, W. Zhang, *Microporous Mesoporous Mater.* **2019**, *288*, 109555.
[91] K. G. Haw, J. P. Gilson, N. Nesterenko, M. Akouche, H. El Siblani, J. M. Goupil, B. Rigaud, D. Minoux, J. P. Dath, V. Valtchev, *ACS Catal.* **2018**, *8*, 8199.
[92] E. Dib, H. El Siblani, S. M. Kunjir, A. Vicente, N. Nuttens, D. Verboekend, B. F. Sels, C. Fernandez, *Cryst. Growth Des.* **2018**, *18*, 2010.
[93] X. Li, X. Chen, Z. Yang, X. Zhu, S. Xu, S. Xie, S. Liu, X. Liu, L. Xu, *Microporous Mesoporous Mater.* **2018**, *257*, 79.
[94] Y. Hu, M. Li, G. Hou, S. Xu, K. Gong, X. Liu, X. Han, X. Pan, X. Bao, *Nano Res.* **2018**, *11*, 360.
[95] J. Hunger, I. A. Beta, H. Böhlig, C. Ling, H. Jobic, B. Hunger, *J. Phys. Chem. B* **2006**, *110*, 342.
[96] A. Di Lella, N. Desbiens, A. Boutin, I. Demachy, P. Ungerer, J.-P. Bellat, A. H. Fuchs, *Phys. Chem. Chem. Phys.* **2006**, *8*, 5396.
[97] B. Grünberg, T. Emmler, E. Gedat, I. Shenderovich, G. H. Findenegg, H.-H. Limbach, G. Buntkowsky, *Chemistry* **2004**, *10*, 5689.
[98] H. Uhlig, J. Hollenbach, M. Rogaczewski, J. Matysik, F. J. Brieler, M. Fröba, D. Enke, *Chem. Ing. Tech.* **2017**, *89*, 863.
[99] J. Hollenbach, C. Küster, H. Uhlig, M. Wagner, B. Abel, R. Gläser, W.-D. Einicke, D. Enke, J. Matysik, *J. Phys. Chem. C* **2017**, *121*, 15804.
[100] P. Ruckdeschel, T. W. Kemnitzer, F. A. Nutz, J. Senker, M. Retsch, *Nanoscale* **2015**, *7*, 10059.
[101] N. Mnasri, C. Charnay, L. C. de Ménorval, E. Elaloui, J. Zajac, *J. Solid State Chem.* **2016**, *243*, 207.
[102] K. Bärwinkel, M. M. Herling, M. Rieß, H. Sato, L. Li, Y. S. Avadhut, T. W. Kemnitzer, H. Kalo, J. Senker, R. Matsuda, S. Kitagawa, J. Breu, *J. Am. Chem. Soc.* **2017**, *139*, 904.
[103] M. A. Springuel-Huet, A. Nossov, Z. Adem, F. Guenneau, C. Volkringer, T. Loiseau, G. Férey, A. Gédéon, *J. Am. Chem. Soc.* **2010**, *132*, 11599.
[104] T. W. Kemnitzer, C. B. L. Tschense, T. Wittmann, E. A. Rössler, J. Senker, *Langmuir* **2018**, *34*, 12538.
[105] K. Trepte, J. Schaber, S. Schwalbe, F. Drache, I. Senkovska, S. Kaskel, J. Kortus, E. Brunner, G. Seifert, *Phys. Chem. Chem. Phys.* **2017**, *19*, 10020.

[106] K. Trepte, S. Schwalbe, J. Schaber, S. Krause, I. Senkovska, S. Kaskel, E. Brunner, J. Kortus, G. Seifert, *Phys. Chem. Chem. Phys.* **2018**, *20*, 25039.
[107] R. Giovine, C. Volkringer, M. A. Springuel-Huet, A. Nossov, F. Blanc, J. Trébosc, T. Loiseau, J. P. Amoureux, O. Lafon, F. Pourpoint, *J. Phys. Chem. C* **2017**, *121*, 19262.
[108] S. Leubner, R. Stäglich, J. Franke, J. Jacobsen, J. Gosch, R. Siegel, H. Reinsch, G. Maurin, J. Senker, P. G. Yot, N. Stock, *Chemistry* **2020**, *26*, 3877.
[109] H. Bunzen, F. Kolbe, A. Kalytta-Mewes, G. Sastre, E. Brunner, D. Volkmer, *J. Am. Chem. Soc.* **2018**, *140*, 10191.
[110] M. Fischer, J. Schwegler, C. Paula, P. S. Schulz, M. Hartmann, *Dalton Trans.* **2016**, *45*, 18443.
[111] Y. Z. Chen, B. Gu, T. Uchida, J. Liu, X. Liu, B. J. Ye, Q. Xu, H. L. Jiang, *Nat. Commun.* **2019**, *10*, 3462.
[112] M. L. Díaz-Ramírez, E. Sánchez-González, J. R. Álvarez, G. A. González-Martínez, S. Horike, K. Kadota, K. Sumida, E. González-Zamora, M. A. Springuel-Huet, A. Gutiérrez-Alejandre, V. Jancik, S. Furukawa, S. Kitagawa, I. A. Ibarra, E. Lima, *J. Mater. Chem. A* **2019**, *7*, 15101.
[113] S. Krause, V. Bon, I. Senkovska, U. Stoeck, D. Wallacher, D. M. Többens, S. Zander, R. S. Pillai, G. Maurin, F.-X. Coudert, S. Kaskel, *Nature* **2016**, *532*, 348.
[114] J. Schaber, S. Krause, S. Paasch, I. Senkovska, V. Bon, D. M. Többens, D. Wallacher, S. Kaskel, E. Brunner, *J. Phys. Chem. C* **2017**, *121*, 5195.
[115] J. D. Evans, L. Bocquet, F.-X. Coudert, *Chem* **2016**, *1*, 873.
[116] F. Kolbe, S. Krause, V. Bon, I. Senkovska, S. Kaskel, E. Brunner, *Chem. Mater.* **2019**, *31*, 6193.
[117] Q. Zeng, B. Bie, Q. Guo, Y. Yuan, Q. Han, X. Han, M. Chen, X. Zhang, Y. Yang, M. Liu, P. Liu, H. Deng, X. Zhou, *Proc. Natl. Acad. Sci. U. S. A.* **2020**, 202004121.
[118] K. K. Palaniappan, M. B. Francis, A. Pines, D. E. Wemmer, *Isr. J. Chem.* **2014**, *54*, 104.
[119] E. Mari, P. Berthault, *Analyst* **2017**, *142*, 3298.
[120] S. Berens, F. Hillman, H. K. Jeong, S. Vasenkov, *Microporous Mesoporous Mater.* **2019**, *288*, 109603.
[121] Y. X. Ma, Z. J. Li, L. Wei, S. Y. Ding, Y. B. Zhang, W. Wang, *J. Am. Chem. Soc.* **2017**, *139*, 4995.
[122] P. Håkansson, M. A. Javed, S. Komulainen, L. Chen, D. Holden, T. Hasell, A. I. Cooper, P. Lantto, V.-V. Telkki, *Phys. Chem. Chem. Phys.* **2019**, *21*, 24373.
[123] M. Miklitz, S. Jiang, R. Clowes, M. E. Briggs, A. I. Cooper, K. E. Jelfs, *J. Phys. Chem. C* **2017**, *121*, 15211.
[124] L. Chen, P. S. Reiss, S. Y. Chong, D. Holden, K. E. Jelfs, T. Hasell, M. A. Little, A. Kewley, M. E. Briggs, A. Stephenson, K. M. Thomas, J. A. Armstrong, J. Bell, J. Busto, R. Noel, J. Liu, D. M. Strachan, P. K. Thallapally, A. I. Cooper, *Nat. Mater.* **2014**, *13*, 954.
[125] Q. Wei, G. K. Seward, P. A. Hill, B. Patton, I. E. Dimitrov, N. N. Kuzma, I. J. Dmochowski, *J. Am. Chem. Soc.* **2006**, *128*, 13274.
[126] S. Komulainen, J. Roukala, V. V. Zhivonitko, M. A. Javed, L. Chen, D. Holden, T. Hasell, A. I. Cooper, P. Lantto, V. V. Telkki, *Chem. Sci.* **2017**, *8*, 5721.
[127] A. J. Martínez-Martínez, N. H. Rees, A. S. Weller, *Angew. Chem., Int. Ed.* **2019**, *58*, 16873.
[128] M. Selent, J. Nyman, J. Roukala, M. Ilczyszyn, R. Oilunkaniemi, P. J. Bygrave, R. Laitinen, J. Jokisaari, G. M. Day, P. Lantto, *Chemistry* **2017**, *23*, 5258.
[129] Y. Kudo, H. Mikami, M. Tanaka, T. Isaji, K. Odaka, M. Yamato, H. Kawakami, *J. Memb. Sci.* **2020**, *597*, 117627.
[130] Y. Mao, M. Song, R. Hopson, N. K. Karan, P. R. Guduru, L. Q. Wang, *Energy Fuels* **2016**, *30*, 1470.
[131] Y. Mao, N. K. Karan, M. Song, R. Hopson, P. R. Guduru, L. Q. Wang, *Energy Fuels* **2017**, *31*, 5622.
[132] S. Xu, X. Li, C. Sun, A. Zheng, W. Zhang, X. Han, X. Liu, X. Bao, *Phys. Chem. Chem. Phys.* **2019**, *21*, 3287.
[133] A. Clough, J. L. Sigle, D. Jacobi, J. Sheremata, J. L. White, *Energy Fuels* **2015**, *29*, 6370.
[134] M. A. Javed, S. Komulainen, H. Daigle, B. Zhang, J. Vaara, B. Zhou, V. V. Telkki, *Microporous Mesoporous Mater.* **2019**, *281*, 66.
[135] A. Puente-Urbina, J. Hollenbach, I. F. Céspedes-Camacho, J. Matysik, G. Valle-Bourrouet, *J. Porous Mater.* **2016**, *23*, 1439.
[136] M. Farina, M. Mauri, G. Patriarca, R. Simonutti, K. T. Klasson, H. N. Cheng, *RSC Adv.* **2016**, *6*, 103803.
[137] V. V. Zhivonitko, A. I. Svyatova, K. V. Kovtunov, I. V. Koptyug, in *Annual Reports of NMR Spectroscopy* (Ed.: G. A. Webb), Elsevier, Amsterdam **2018**, pp. 83–145.
[138] A. Svyatova, E. S. Kononenko, K. V. Kovtunov, D. Lebedev, E. Y. Gerasimov, A. V. Bukhtiyarov, I. P. Prosvirin, V. I. Bukhtiyarov, C. R. Müller, A. Fedorov, I. V. Koptyug, *Catal. Sci. Technol.* **2020**, *10*, 99.
[139] D. B. Burueva, E. V. Pokochueva, X. Wang, M. Filkins, A. Svyatova, S. P. Rigby, C. Wang, G. E. Pavlovskaya, K. V. Kovtunov, T. Meersmann, I. V. Koptyug, *ACS Catal.* **2020**, *10*, 1417.
[140] T. L. Greaves, C. J. Drummond, *Chem. Rev.* **2008**, *108*, 206.
[141] G. Saielli, A. Bagno, F. Castiglione, R. Simonutti, M. Mauri, A. Mele, *J. Phys. Chem. B* **2014**, *118*, 13963.
[142] F. Castiglione, R. Simonutti, M. Mauri, A. Mele, *J. Phys. Chem. Lett.* **2013**, *4*, 1608.
[143] P. Morgado, K. Shimizu, J. M. S. S. Esperança, P. M. Reis, L. P. N. Rebelo, J. N. C. Lopes, E. J. M. Filipe, *J. Phys. Chem. Lett.* **2013**, *4*, 2758.
[144] N. J. Brooks, F. Castiglione, C. M. Doherty, A. Dolan, A. J. Hill, P. A. Hunt, R. P. Matthews, M. Mauri, A. Mele, R. Simonutti, I. J. Villar-Garcia, C. C. Weber, T. Welton, *Chem. Sci.* **2017**, *8*, 6359.
[145] C. C. Weber, N. J. Brooks, F. Castiglione, M. Mauri, R. Simonutti, A. Mele, T. Welton, *Phys. Chem. Chem. Phys.* **2019**, *21*, 5999.
[146] F. Castiglione, G. Saielli, M. Mauri, R. Simonutti, A. Mele, *J. Phys. Chem. B* **2020**, *124*, 6617.
[147] M. T. Heinze, J. C. Zill, J. Matysik, W. D. Einicke, R. Gläser, A. Stark, *Phys. Chem. Chem. Phys.* **2014**, *16*, 24359.
[148] K. A. Cychosz, M. Thommes, *Engineering* **2018**, *4*, 559.
[149] L. Q. Wang, A. Karkamkar, T. Autrey, G. J. Exarhos, *J. Phys. Chem. C* **2009**, *113*, 6485.
[150] F. Guenneau, K. Panesar, A. Nossov, M.-A. Springuel-Huet, T. Azaïs, F. Babonneau, C. Tourné-Péteilh, J.-M. Devoisselle, A. Gédéon, *Phys. Chem. Chem. Phys.* **2013**, *15*, 18805.

Dorothea Wisser obtained her Ph.D. in 2015 in solid-state NMR of materials at the Dresden University of Technology. She worked as a postdoctoral fellow at the European High Field NMR Center Lyon (CRMN) and the IFP Energies Nouvelles Solaize. Her research is focused on the MAS NMR investigation of structures and interfaces of advanced materials and method development in dynamic nuclear polarization NMR. Since 2019, she is group leader for solid-state NMR at the Erlangen Center for Interface Research and Catalysis at the Friedrich-Alexander University Erlangen-Nürnberg.

Martin Hartmann obtained his Ph.D. in physical chemistry in 1993. He held postdoctoral positions at the University of Houston (1994–1995), University of Stuttgart (1996–1999) finished his habilitation in Chemical Technology at TU Kaiserslautern in 2002. In 2005, he became professor of advanced materials science at the University of Augsburg. He joined the Friedrich-Alexander-University of Erlangen-Nürnberg (FAU) in 2009 as professor of catalysis and director of the Erlangen Center of Interface Research and Catalysis (ECRC). His research interests focus on the synthesis and spectroscopic characterization of porous materials for applications in catalysis, separation, and energy storage.